electronics

MDPI

Article

An Adaptive Finite Element/Finite Difference Domain Decomposition Method for Applications in Microwave Imaging

Larisa Beilina [1,2,*] and Eric Lindström [1,2]

[1] Department of Mathematical Sciences, Chalmers University of Technology, 41296 Gothenburg, Sweden; erilinds@chalmers.se
[2] Department of Mathematical Sciences, Gothenburg University, 41296 Gothenburg, Sweden
* Correspondence: larisa@chalmers.se

Abstract: A new domain decomposition method for Maxwell's equations in conductive media is presented. Using this method, reconstruction algorithms are developed for the determination of the dielectric permittivity function using time-dependent scattered data of an electric field. All reconstruction algorithms are based on an optimization approach to find the stationary point of the Lagrangian. Adaptive reconstruction algorithms and space-mesh refinement indicators are also presented. Our computational tests show the qualitative reconstruction of the dielectric permittivity function using an anatomically realistic breast phantom.

Keywords: Maxwell's equations; conductive media; microwave imaging; coefficient inverse problem; adaptive finite element method; finite difference method; domain decomposition

MSC: 65M06; 65M32; 65M55; 65M60

Citation: Beilina, L.; Lindström, E. An Adaptive Finite Element/Finite Difference Domain Decomposition Method for Applications in Microwave Imaging. *Electronics* **2022**, *11*, 1359. https://doi.org/10.3390/electronics11091359

Academic Editors: Gian Luigi Gragnani and Alessandro Fedeli

Received: 11 March 2022
Accepted: 21 April 2022
Published: 24 April 2022

1. Introduction

In this work are presented reconstruction algorithms for the problem of the determination of the spatially distributed dielectric permittivity function in conductive media using scattered time-dependent data of the electric field at the boundary of the investigated domain. Such problems are called Coefficient Inverse Problems (CIPs). A CIP for a system of time-dependent Maxwell's equations for an electric field is a problem regarding the reconstruction of the unknown spatially distributed coefficients of this system from boundary measurements.

One of the most important applications of the algorithms of this paper is microwave imaging, including microwave medical imaging and the imaging of improvised explosive devices (IEDs). Potential applications of the algorithms developed in this work are in breast cancer detection. In the numerical examples of the current paper, we focus on the microwave medical imaging of a realistic breast phantom provided by an online repository [1]. In this work, we develop simplified versions of reconstruction algorithms, which allow us to determine the dielectric permittivity function under the condition that the effective conductivity function is known. Currently, we are working on the development of similar algorithms for the determination of both spatially distributed functions, dielectric permittivity and conductivity, and we are planning a report about the obtained results in the near future.

Microwave medical imaging is non-invasive imaging. Thus, it is a very attractive addition to the existing imaging technologies, such as X-ray mammography, ultrasound and MRI imaging. It makes use of the capability of microwaves to differentiate among tissues based on the contrast in their dielectric properties. In [2] were reported different malign-to-normal tissue contrasts, revealing that malign tumors have a higher water/liquid content and, thus, higher relative permittivity and conductivity values than normal tissues. The challenge is to accurately estimate the relative permittivity of the internal structures

using the information from the backscattered electromagnetic waves of frequencies around 1 GHz collected at several detectors.

Since the 1990s, quantitative reconstruction algorithms based on the solution of CIPs for Maxwell's system have been developed to provide images of the complex permittivity function; see [3] for 2D techniques, [4–7] for 3D techniques in the frequency domain and [8,9] for time-domain (TD) techniques. In all these works, microwave medical imaging remains the research field and has little clinical acceptance [10] since the computations are inefficient, take too long and produce low contrast values for the inside inclusions. In all the above-cited works, local gradient-based mathematical algorithms use frequency-dependent measurements, which often produce low contrast values of inclusions and miss small cancerous inclusions. Moreover, computations in these algorithms are done often in MATLAB, sometimes requiring around 40 h for the solution of inverse problems.

It is well known that CIPs are ill-posed problems [11–14]. The development of non-local numerical methods is the main challenge in the solution of such problems. In works [15–18], the authors developed and numerically verified a new, non-local, approximately globally convergent method for the reconstruction of the dielectric permittivity function. The two-stage global adaptive optimization method was developed in [15] for the reconstruction of the dielectric permittivity function. The two-stage numerical procedure of [15] was verified in several works [16–18] on experimental data collected by the microwave scattering facility. The experimental and numerical tests of the above-cited works show that the developed methods provide accurate imaging of all three components of interest in the imaging of targets: shapes, locations and refractive indices of non-conductive media. In [7]—see also the references therein—the authors show the reconstruction of the complex dielectric permittivity function using the convexification method and frequency-dependent data. Potential applications of all the above-cited works are in the detection and characterization of improvised explosive devices (IEDs).

The algorithms of the current work can efficiently and accurately reconstruct the dielectric permittivity function in conductive media using time-dependent measurements of the electric field for one concrete frequency using single-measurement data generated by a plane wave. A plane wave can be generated by a horn antenna, as was done in experimental works [16–18]. We are aware that the conventional measurement configuration for the detection of breast cancer consists of antennas placed on the breast skin [5,8,10,19,20]. In this work, we use another measurement set-up: we assume that the breast is placed in a coupling media and then one component of a time-dependent electric plane wave is initialized at the boundary of the media. Then, scattered data are collected at the transmitted boundary. These data are used in the reconstruction algorithms developed in this work. Such an experimental set-up allows us to avoid multiple measurements and overdetermination since we are working with data resulting from a single measurement. An additional advantage is that, in the case of single-measurement data, one can use the method of Carleman estimates [21] to prove the uniqueness of the reconstruction of the dielectric permittivity function.

For the numerical solution of Maxwell's equations, we have developed a finite element/finite difference domain decomposition method (FE/FD DDM). This approach combines the flexibility of the finite elements and the efficiency of the finite differences in terms of speed and memory usage, as well as fitting the best for the reconstruction algorithms of this paper. We are unaware of other works that use a similar set-up for the solution of CIPs for time-dependent Maxwell's equations in conductive media solved via FE/FD DDM, so this is the first work on this topic.

An outline of the work is as follows: in Section 2, we present the mathematical model, and in Section 3, we describe the structure of domain decomposition. Section 4 presents the reconstruction algorithms, including the formulation of the inverse problem, derivation of finite element and finite difference schemes, together with the optimization approach for the solution of the inverse problem. Section 5 shows numerical examples of the reconstruction of the dielectric permittivity function of an anatomically realistic breast

phantom at frequency 6 GHz from an online repository [1]. Finally, Section 6 discusses the obtained results and future research.

2. The Mathematical Model

Our basic model is given in terms of the electric field $E(x,t) = (E_1, E_2, E_3)(x,t), x \in \mathbb{R}^3$, changing in the time interval $t \in (0,T)$, under the assumption that the dimensionless relative magnetic permeability of the medium is $\mu_r \equiv 1$. We consider the Cauchy problem for the Maxwell equations for electric field $E(x,t)$, further assuming that the electric volume charges are equal to zero, to obtain the model equation for $x \in \mathbb{R}^3, t \in (0,T]$.

$$\begin{aligned} \frac{1}{c^2}\varepsilon_r \frac{\partial^2 E}{\partial t^2} + \nabla \times \nabla \times E &= -\mu_0 \sigma \frac{\partial E}{\partial t}, \\ \nabla \cdot (\varepsilon E) &= 0, \\ E(\cdot,0) = f_0, \quad \frac{\partial E}{\partial t}(\cdot,0) &= f_1. \end{aligned} \tag{1}$$

Here, $\varepsilon_r(x) = \varepsilon(x)/\varepsilon_0$ is the dimensionless relative dielectric permittivity and $\sigma(x)$ is the effective conductivity function; ε_0, μ_0 are the permittivity and permeability of the free space, respectively, and $c = 1/\sqrt{\varepsilon_0 \mu_0}$ is the speed of light in free space.

We are not able to numerically solve the problem (1) in the unbounded domain, and thus we introduce a convex bounded domain $\Omega \subset \mathbb{R}^3$ with boundary $\partial\Omega$. For the numerical solution of the problem (1), a domain decomposition finite element/finite difference method is developed and summarized in Algorithm 1.

Algorithm 1: The domain decomposition algorithm.

1: On the structured part of the mesh Ω_{FDM}, where FDM is used, update the finite difference (FD) solution at nodes ω_+ and $\omega_\diamond$.
2: On the unstructured part of the mesh Ω_{FEM}, where FEM is used, update the finite element (FE) solution at nodes ω_* and ω_{o}.
3: Copy the FE solution obtained at nodes $\omega_\diamond$ as a boundary condition for the FD solution in Ω_{FDM}.
4: Copy the FD solution obtained at nodes ω_{o} as a boundary condition for the FE solution in Ω_{FEM}.

A domain decomposition means that we divide the computational domain Ω into two subregions, Ω_{FEM} and Ω_{FDM}, such that $\Omega = \Omega_{\mathrm{FEM}} \cup \Omega_{\mathrm{FDM}}$ with $\Omega_{\mathrm{FEM}} \subset \Omega$; see Figure 1. Moreover, we additionally decompose the domain $\Omega_{\mathrm{FEM}} = \Omega_{\mathrm{IN}} \cup \Omega_{\mathrm{OUT}}$ with $\Omega_{\mathrm{IN}} \subset \Omega_{\mathrm{FEM}}$ such that functions $\varepsilon_r(x)$ and $\sigma(x)$ of Equation (1) should be determined only in Ω_{IN}; see Figure 2. When solving the inverse problem this assumption allows stable computation of the unknown functions $\varepsilon_r(x)$ and $\sigma(x)$ even if they have large discontinuities in Ω_{FEM}.

The communication between Ω_{FEM} and Ω_{FDM} is arranged using a mesh overlapping through a two-element-thick layer around Ω_{FEM}; see the elements in the blue color in Figure 1a,b. This layer consists of triangles in $\mathbb{R}^2$ or tetrahedrons in $\mathbb{R}^3$ for Ω_{FEM}, and of squares in $\mathbb{R}^2$ or cubes in $\mathbb{R}^3$ for Ω_{FDM}.

The key idea with such a domain decomposition is to apply different numerical methods in different computational domains. For the numerical solution of (1) in Ω_{FDM}, we use the finite difference method on a structured mesh. In Ω_{FEM}, we use finite elements on a sequence of unstructured meshes $K_h = \{K\}$, with elements K consisting of tetrahedrons in $\mathbb{R}^3$, satisfying the minimal angle condition [22].

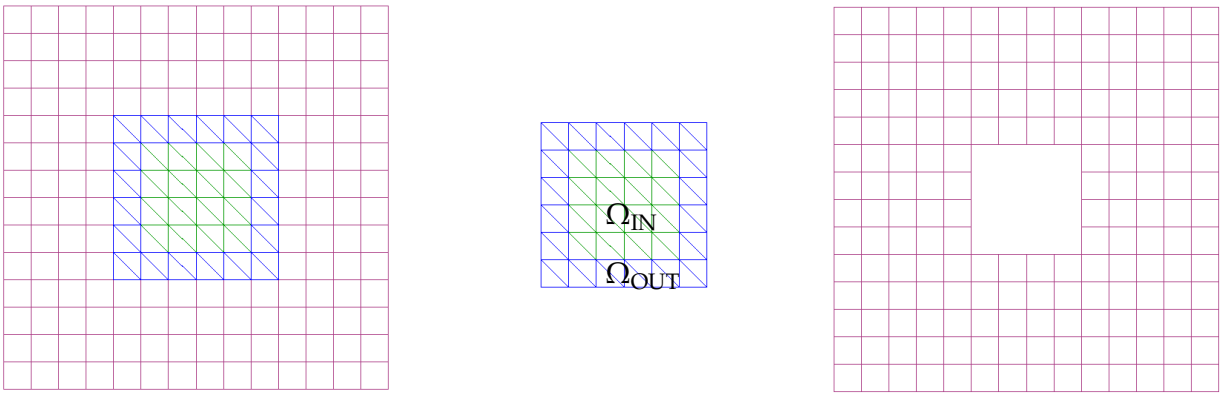

(**a**) $\Omega = \Omega_{FEM} \cup \Omega_{FDM}$ (**b**) $\Omega_{FEM} = \Omega_{IN} \cup \Omega_{OUT}$ (**c**) Ω_{FDM}

Figure 1. Domain decomposition and mesh discretization in Ω. The domain Ω presented in (**a**) is a combination of the quadrilateral finite difference mesh Ω_{FDM} presented in (**c**) and the finite element mesh Ω_{FEM} presented in (**b**).

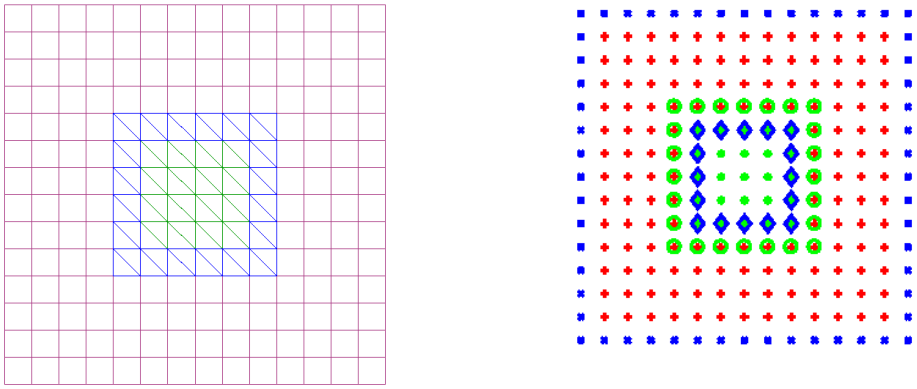

(**a**) $\Omega = \Omega_{FEM} \cup \Omega_{FDM}$ (**b**) $\Omega = \Omega_{FEM} \cup \Omega_{FDM}$

Figure 2. Coupling between Ω_{FEM} and Ω_{FDM}. The nodes of the FE/FD mesh of (**a**) are presented also on (**b**) as sets of the following nodes: ω_o (green circles), $\omega_\diamond$ (blue diamonds), ω_* (green stars), ω_+ (red pluses), ω_x (blue crosses). These sets are described in the domain decomposition algorithm.

We assume in this paper that, for some known constants $d_1 > 1, d_2 > 0$, the functions $\varepsilon_r(x)$ and $\sigma(x)$ of Equation (1) satisfy

$$\begin{aligned} &\varepsilon_r(x) \in [1, d_1], \quad \sigma(x) \in [0, d_2], \ \text{ for } x \in \Omega_{IN}, \\ &\varepsilon_r(x) = 1, \quad \sigma(x) = 0 \quad \text{ for } x \in \Omega_2 \cup \Omega_{OUT}, \ \ \varepsilon_r(x), \sigma(x) \in C^2\left(\mathbb{R}^3\right). \end{aligned} \tag{2}$$

Turning to the boundary conditions at $\partial\Omega$, we use the fact that (2) and (1) imply that since $\varepsilon_r(x) = 1, \sigma(x) = 0$ for $x \in \Omega_{FDM} \cup \Omega_{OUT}$, then a well-known transformation

$$\nabla \times \nabla \times E = \nabla(\nabla \cdot E) - \nabla \cdot (\nabla E) \tag{3}$$

makes the terms in Equation (1) independent of each other in Ω_{FDM}, and thus, in Ω_{FDM}, we need to solve the equation

$$\frac{\partial^2 E}{\partial t^2} - \Delta E = 0, \quad (x, t) \in \Omega_{FDM} \times (0, T]. \tag{4}$$

We write $\partial\Omega = \partial\Omega_1 \cup \partial\Omega_2 \cup \partial\Omega_3$, meaning that $\partial\Omega_1$ and $\partial\Omega_2$ are the top and bottom sides of the domain Ω, while $\partial\Omega_3$ is the rest of the boundary. Because of (4), it seems natural to impose a first-order absorbing boundary condition for the wave equation [23],

$$\frac{\partial E}{\partial n} + \frac{\partial E}{\partial t} = 0, (x,t) \in \partial\Omega \times (0,T]. \tag{5}$$

Here, we denote the outer normal derivative of the electrical field on $\partial\Omega$ by $\frac{\partial \cdot}{\partial n}$, where n denotes the unit outer normal vector on $\partial\Omega$.

It is well known that, for the stable implementation of the finite element solution of Maxwell's equation, divergence-free edge elements are the most satisfactory from a theoretical point of view [24,25]. However, the edge elements are less attractive for the solution of time-dependent problems since a linear system of equations should be solved at every time iteration. In contrast, P1 elements can be efficiently used in a fully explicit finite element scheme with a lumped mass matrix [26,27]. It is also well known that the numerical solution of Maxwell's equations using nodal finite elements can result in unstable spurious solutions [28,29]. There are a number of techniques that are available to remove them; see, for example, [29–33].

In the domain decomposition method of this work, we use the stabilized P1 FE method for the numerical solution of (1) in Ω_{FEM}. The efficiency of using an explicit P1 finite element scheme is evident for the solution of CIPs. In many algorithms that solve electromagnetic CIPs, a qualitative collection of experimental measurements is necessary on the boundary of the computational domain to determine the dielectric permittivity function inside it. In this case, the numerical solutions of time-dependent Maxwell's equations are required in the entire space $\mathbb{R}^3$—see, for example, [15–18,34]—and it is efficient to consider Maxwell's equations with a constant dielectric permittivity function in a neighborhood of the boundary of the computational domain. An explicit P1 finite element scheme with $\sigma = 0$ in (1) is numerically tested for the solution of the time-dependent Maxwell's system in 2D and 3D in [35]. Convergence analysis of this scheme is presented in [36]; see also references therein for the CFL condition for this scheme. The scheme of [35] is used for the solution of different CIPs for the determination of the dielectric permittivity function in non-conductive media in time-dependent Maxwell's equations using simulated and experimentally generated data; see [16–18,34].

The stabilized model problem considered in this paper is

$$\begin{array}{ll} \frac{1}{c^2}\varepsilon_r \frac{\partial^2 E}{\partial t^2} + \nabla(\nabla \cdot E) - \triangle E - \varepsilon_0 \nabla(\nabla \cdot (\varepsilon_r E)) = -\mu_0 \sigma \frac{\partial E}{\partial t} & \text{in } \Omega \times (0,T), \\ E(\cdot,0) = f_0, \text{ and } \frac{\partial E}{\partial t}(\cdot,0) = f_1 & \text{in } \Omega, \\ \frac{\partial E}{\partial n} = -\frac{\partial E}{\partial t} & \text{on } \partial\Omega \times (0,T), \end{array} \tag{6}$$

with functions ε_r, σ satisfying condition (2).

3. The Domain Decomposition Algorithm

We now describe the domain decomposition method between two domains Ω_{FEM} and Ω_{FDM}, where FEM is used for the computation of the solution in Ω_{FEM}, and FDM is used in Ω_{FDM}; see Figures 1 and 2. Overlapping nodes between Ω_{FDM} and Ω_{FEM} are outlined in Figure 2 by green circles (boundary nodes of Ω_{FEM}) and blue diamonds (inner boundary nodes of Ω_{FDM}).

The communication between two domains Ω_{FEM} and Ω_{FDM} is achieved by the overlapping of both meshes across a two-element-thick layer around Ω_{FEM}—see Figure 2. The nodes of the computational domain Ω belong to one of the following sets (see Figure 2b):

ω_{o}: Nodes 'o' lie on the boundary $\partial\Omega_{\text{FEM}}$ of Ω_{FEM} and are interior to Ω_{FDM};
$\omega_{\diamond}$: Nodes '$\diamond$' lie on the inner boundary $\partial\Omega_{\text{FDM}}$ of Ω_{FDM} and are interior to Ω_{FEM};
ω_{*}: Nodes '$*$' are interior to Ω_{FEM};
ω_{+}: Nodes '$+$' are interior to Ω_{FDM};
ω_{x}: Nodes 'x' lie on the outer boundary $\partial\Omega$ of Ω_{FDM}.

Then, the main loop in time for the explicit schemes that solve the problem (6) with appropriate boundary conditions is shown in Algorithm 1.

By condition (2), functions $\varepsilon_r = 1$ and $\sigma = 0$ at the overlapping nodes between Ω_{FEM} and Ω_{FDM}, and thus the Maxwell's equations, will transform to the system of uncoupled acoustic wave Equation (4), which leads to the fact that the FEM and FDM discretization schemes coincide on the common structured overlapping layer. In this way, we avoid instabilities at interfaces in the domain decomposition algorithm.

4. Reconstruction Algorithms

In this section, we develop different optimization algorithms that allow the determination of the relative dielectric permittivity function using scattered data of the electric field at the boundary of the investigated domain. In all algorithms, we use the assumption that the effective conductivity function is known in the investigated domain.

In summary, the main algorithms presented in this section are:

- Algorithm 2: The domain decomposition algorithm for the efficient solution of forward and adjoint problems used in Algorithms 3–5.
- Algorithm 3: Optimization algorithm for the determination of the relative dielectric permittivity function under the condition that the effective conductivity function is known.
- Algorithms 4 and 5: Adaptive optimization algorithms for the determination of the relative dielectric permittivity function. These algorithms use local adaptive mesh refinement based on a new error indicator for the improved determination of the location, material and sizes of the inclusions to be identified.

Let the domain decomposition of the computational domain Ω be as it is described in Section 3; see also Figure 2. We denote by $\Omega_T := \Omega \times (0,T), \partial\Omega_T := \partial\Omega \times (0,T), T > 0$. Let the boundary $\partial\Omega = \partial\Omega^{\text{out}}_{\text{FDM}} \cup \partial\Omega^{\text{in}}_{\text{FDM}}$ be the outer boundary $\partial\Omega^{\text{out}}_{\text{FDM}}$ of Ω together with the inner boundary $\partial\Omega^{\text{in}}_{\text{FDM}}$ of Ω_{FDM}, and $\partial\Omega_{\text{FEM}}$ be the boundary of Ω_{FEM}. At $S_T := \partial\Omega^{\text{out}}_{\text{FDM}} \times (0,T)$, we have time-dependent backscattering observations.

Our coefficient inverse problem will be the following.

Inverse Problem (IP) *Assume that the functions $\varepsilon_r(x)$, $\sigma(x)$ satisfy condition (2) for known $d_1 > 1$, $d_2 > 0$. Let the function ε_r be unknown in the domain $\Omega \backslash (\Omega_{\text{FDM}} \cup \Omega_{\text{OUT}})$. Determine the function $\varepsilon_r(x)$ for $x \in \Omega \backslash (\Omega_{\text{FDM}} \cup \Omega_{\text{OUT}})$, assuming that the function $\sigma(x)$ is known in Ω and the following function $\tilde{E}(x,t)$ is measured at S_T:*

$$E(x,t) = \tilde{E}(x,t), \forall (x,t) \in S_T. \tag{7}$$

The function $\tilde{E}(x,t)$ in (7) represents the time-dependent measurements of all components of the electric wave field $E(x,t) = (E_1, E_2, E_3)(x,t)$ at S_T.

To solve IP, we minimize the corresponding Tikhonov functional using a Lagrangian approach. We present details of the derivation of the optimization algorithms in the next section.

4.1. Derivation of Optimization Algorithms

For the solution of the **IP** for Maxwell's system (6), it is natural to minimize the following Tikhonov functional:

$$J(E, \varepsilon_r) = \frac{1}{2} \int_{S_T} (E - \tilde{E})^2 z_\delta \, dsdt + \frac{1}{2} \gamma \int_\Omega (\varepsilon_r - \varepsilon^0)^2 \, dx, \tag{8}$$

where $\tilde{E}$ is the observed electric field in (7), and E satisfies Equation (6) and thus depends on ε_r, σ. We denote by ε^0 the initial guess for ε_r, and by γ the regularization parameter. Here, z_δ is a cut-off function ensuring the compatibility conditions for data; see details in [34].

Let us introduce the following spaces of real valued functions:

$$\begin{aligned} H_E^1(\Omega_T) &:= \{w \in H^1(\Omega_T) : w(\cdot,0) = 0\}, \\ H_\lambda^1(\Omega_T) &:= \{w \in H^1(\Omega_T) : w(\cdot,T) = 0\}, \\ U^1 &= ((H_E^1(\Omega_T)^3 \times (H_E^1(\Omega_T))^3 \times C(\overline{\Omega}), \\ U^0 &= (L_2(\Omega_T))^3 \times (L_2(\Omega_T))^3 \times L_2(\Omega). \end{aligned} \tag{9}$$

To solve the minimization problem

$$\min_{\varepsilon_r} J(E, \varepsilon_r) \tag{10}$$

we take into account condition (2) on the function ε_r and introduce the Lagrangian

$$\begin{aligned} L(u) &= J(E, \varepsilon_r) \\ &+ \int_{\Omega_T} \lambda \Big(\frac{1}{c^2} \varepsilon_r \frac{\partial^2 E}{\partial t^2} - \nabla \cdot (\nabla E) - \nabla \nabla \cdot ((\varepsilon_r \varepsilon_0 - 1)E) + \mu_0 \sigma \frac{\partial E}{\partial t} \Big) \, dxdt, \end{aligned} \tag{11}$$

where $u = (E, \lambda, \varepsilon_r)$.

To solve the minimization problem (10), we find a stationary point of the Lagrangian with respect to u satisfying $\forall \bar{u} = (\bar{E}, \bar{\lambda}, \bar{\varepsilon_r}) \in U^1$

$$L'(u; \bar{u}) = 0, \tag{12}$$

where $L'(u; \cdot)$ is the Jacobian of L at u. For the solution of the minimization problem (12), we develop a conjugate gradient method for the reconstruction of parameter ε_r.

To obtain optimality conditions from (12), we integrate by parts in space and time the Lagrangian (11), assuming that $\lambda(x,T) = \frac{\partial \lambda}{\partial t}(x,T) = 0$, $\frac{\partial \lambda}{\partial t} = \frac{\partial \lambda}{\partial n}$, and impose such conditions on the function λ that $L(E, \lambda, \varepsilon_r) := L(u) = J(E, \varepsilon_r)$. Using the facts that $\lambda(x,T) = \frac{\partial \lambda}{\partial t}(x,T) = 0$ and $\sigma = 0, \varepsilon_r = 1$ on $\partial\Omega$, together with the initial and boundary conditions of (6), we obtain the following optimality conditions for all $\bar{u} \in U^1$:

$$\begin{aligned} 0 = \frac{\partial L}{\partial \lambda}(u)(\bar{\lambda}) &= -\int_{\Omega_T} \frac{1}{c^2} \varepsilon_r \frac{\partial \bar{\lambda}}{\partial t} \frac{\partial E}{\partial t} \, dxdt + \int_{\Omega_T} (\nabla E)(\nabla \bar{\lambda}) \, dxdt \\ &+ \varepsilon_0 \int_{\Omega_T} (\nabla \cdot (\varepsilon_r E))(\nabla \cdot \bar{\lambda}) \, dxdt - \int_{\Omega_T} (\nabla \cdot E)(\nabla \cdot \bar{\lambda}) \, dxdt \\ &+ \int_{\Omega_T} \mu_0 \sigma \frac{\partial E}{\partial t} \bar{\lambda} \, dxdt - \int_\Omega \frac{\varepsilon_r}{c^2} \bar{\lambda}(x,0) f_1(x) \, dx \\ &+ \int_{\partial\Omega_T} \bar{\lambda} \frac{\partial E}{\partial t} \, d\sigma dt, \ \ \forall \bar{\lambda} \in (H_\lambda^1(\Omega_T)^3); \end{aligned} \tag{13}$$

$$\begin{aligned} 0 = \frac{\partial L}{\partial E}(u)(\bar{E}) &= \int_{S_T} (E - \widetilde{E}) \, \bar{E} \, z_\delta \, d\sigma dt - \int_\Omega \frac{\varepsilon_r}{c^2} \frac{\partial \lambda}{\partial t}(x,0) \bar{E}(x,0) \, dx \\ &- \int_{\partial\Omega_T} \frac{\partial \lambda}{\partial t} \bar{E} \, d\sigma dt - \int_{\Omega_T} \frac{\varepsilon_r}{c^2} \frac{\partial \lambda}{\partial t} \frac{\partial \bar{E}}{\partial t} \, dxdt + \int_{\Omega_T} (\nabla \lambda)(\nabla \bar{E}) \, dxdt \\ &+ \varepsilon_0 \int_{\Omega_T} (\nabla \cdot (\varepsilon_r \bar{E}))(\nabla \cdot \lambda) \, dxdt - \int_{\Omega_T} (\nabla \cdot \bar{E})(\nabla \cdot \lambda) \, dxdt \\ &- \int_{\Omega_T} \mu_0 \sigma \bar{E} \frac{\partial \lambda}{\partial t} \, dxdt, \ \forall \bar{E} \in (H_E^1(\Omega_T)^3). \end{aligned} \tag{14}$$

Finally, we obtain the main equation for iterative update ε_r in the conjugate gradient algorithm, which express that the gradient with respect to ε_r vanishes:

$$\begin{aligned} 0 = \frac{\partial L}{\partial \varepsilon_r}(u)(\bar{\varepsilon}_r) = -\int_\Omega \frac{\bar{\varepsilon}_r}{c^2}\lambda(x,0)f_1(x)\,dx - \int_{\Omega_T}\frac{\bar{\varepsilon}_r}{c^2}\frac{\partial\lambda}{\partial t}\frac{\partial E}{\partial t}\,dxdt \\ + \varepsilon_0\int_{\Omega_T}(\nabla\cdot\lambda)(\nabla\cdot(\bar{\varepsilon}_r E))\,dxdt + \gamma\int_\Omega(\varepsilon_r-\varepsilon^0)\bar{\varepsilon}_r\,dx,\ x\in\Omega. \end{aligned} \tag{15}$$

Equation (13) is the weak formulation of the forward problem (6) and Equation (14) is the weak formulation of the following adjoint problem:

$$\begin{array}{ll} \frac{1}{c^2}\varepsilon_r\frac{\partial^2\lambda}{\partial t^2} - \triangle\lambda - \varepsilon_0\varepsilon_r\nabla(\nabla\cdot\lambda) + \nabla(\nabla\cdot\lambda) - \mu_0\sigma\frac{\partial\lambda}{\partial t} = -(E-\widetilde{E})z_\delta & \text{in } \Omega_T, \\ \lambda(\cdot,T) = \frac{\partial\lambda}{\partial t}(\cdot,T) = 0 & \text{in } \Omega, \\ \frac{\partial\lambda}{\partial n} = \frac{\partial\lambda}{\partial t} & \text{on } S_T. \end{array} \tag{16}$$

4.2. The Domain Decomposition FE/FD Method for the Solution of Forward and Adjoint Problems

Finite Element Discretization

We denote by $\Omega_{\mathrm{FEM_T}} := \Omega_{\mathrm{FEM}}\times(0,T), \partial\Omega_{\mathrm{FEM_T}} := \partial\Omega_{\mathrm{FEM}}\times(0,T), T>0$, where $\partial\Omega_{\mathrm{FEM}}$ is the boundary of Ω_{FEM}, and we discretize Ω_{FEM_T}, denoting by $K_h = \{K\}$ a partition of the domain Ω_{FEM} into elements K such that

$$K_h = \cup_{K\in K_h}K = K_1\cup K_2 ... \cup K_l,$$

where l is the total number of elements K in $\overline{\Omega}_{\mathrm{FEM}}$.

Here, $h = h(x)$ is a piecewise-constant mesh function defined as

$$h|_K = h_K \quad \forall K\in K_h, \tag{17}$$

representing the local diameter of the elements. We also denote by $\partial K_h = \{\partial K\}$ a partition of the boundary $\partial\Omega_{\mathrm{FEM}}$ into boundaries ∂K of the elements K such that vertices of these elements belong to $\partial\Omega_{\mathrm{FEM}}$. We let J_τ be a partition of the time interval $(0,T)$ into time intervals $J = (t_{k-1}, t_k]$ of uniform length $\tau = T/N$ for a given number of time steps N. We assume also a minimal angle condition on the K_h [22,37].

To formulate the finite element method in Ω for (12), we define the finite element spaces C_h, W_h^E. First, we introduce the finite element trial space W_h^E for every component of the electric field E defined by

$$W_h^E := \{w\in H_E^1 : w|_K\in P_1(K), \forall K\in K_h\},$$

where $P_1(K)$ denotes the set of piecewise-linear functions on K.

To approximate function ε_r, we define the space of piecewise-constant functions $C_h\subset L_2(\Omega)$,

$$C_h := \{u\in L_2(\Omega) : u|_K\in P_0(K), \forall K\in K_h\}, \tag{18}$$

where $P_0(K)$ is the piecewise-constant function on K. Setting $\mathbf{W}_h^E(\Omega) := [W_h^E(\Omega)]^3$, we define $U_h = \mathbf{W}_h^E(\Omega)\times\mathbf{W}_h^E(\Omega)\times C_h$. The finite element method for (12) now reads as follows: find $u_h\in U_h$, such that

$$L'(u_h)(\bar{u}) = 0,\ \forall\bar{u}\in U_h. \tag{19}$$

Equation (19) expresses discretized versions of the optimality conditions given by (13)–(15). To obtain function ε_r via optimality condition (15), we need solutions first of the forward problem (6), and then of the adjoint problem (16). To solve these problems via the domain decomposition method, we decompose the computational domain

$\Omega = \Omega_{\text{FEM}} \cup \Omega_{\text{FDM}}$ as described in Section 3. Thus, in Ω_{FEM}, we have to solve the following forward problem:

$$\begin{array}{ll} \frac{1}{c^2}\varepsilon_r \frac{\partial^2 E}{\partial t^2} + \nabla(\nabla \cdot E) - \triangle E - \varepsilon_0 \nabla(\nabla \cdot (\varepsilon_r E)) = -\mu_0 \sigma \frac{\partial E}{\partial t} & \text{in } \Omega_{\text{FEM}} \times (0,T), \\ E(\cdot,0) = f_0, \text{ and } \frac{\partial E}{\partial t}(\cdot,0) = f_1 & \text{in } \Omega_{\text{FEM}}, \\ \frac{\partial E}{\partial n} = g & \text{on } \partial\Omega_{\text{FEM}} \times (0,T). \end{array} \tag{20}$$

Here, g is the solution obtained by the finite difference method in Ω_{FDM}, which is saved at $\partial\Omega_{\text{FEM}}$.

Equation (19) expresses that the finite element method in Ω_{FEM} for the solution of the forward problem (20) will be as follows: *Find* $E_h \in \mathbf{W}_h^E(\Omega_{\text{FEM}})$ *such that*

$$\begin{array}{l} \frac{1}{c^2}\left(\varepsilon_{rh}\frac{\partial^2 E_h}{\partial t^2}, \bar{\lambda}\right) + (\nabla E_h, \nabla\bar{\lambda}) + \varepsilon_0(\nabla\cdot(\varepsilon_{rh}E_h), \nabla\cdot\bar{\lambda}) - (\nabla\cdot E_h, \nabla\cdot\bar{\lambda}) \\ +(g_h, \bar{\lambda})_{\partial\Omega_{\text{FEM}}} + \mu_0(\sigma_h \frac{\partial E_h}{\partial t}, \bar{\lambda}) = 0, \;\; \bar{\lambda} \in \mathbf{W}_h^E(\Omega_{\text{FEM}}) \\ E_h(\cdot,0) = f_{0_h} \text{ and } \frac{\partial E_h}{\partial t}(\cdot,0) = f_{1_h} \text{ in } \Omega_{\text{FEM}}. \end{array} \tag{21}$$

Here, we define $f_{0_h}, f_{1_h}, g_h, \varepsilon_{rh}, \sigma_h$ to be the usual $\mathbf{W}_h^E$-interpolate of $f_0, f_1, g, \varepsilon_r, \sigma$ in (6) in Ω_{FEM}.

To obtain the discrete scheme for (21), we approximate $E_h(k\tau)$ by E_h^k for $k = 1, 2, \ldots, N$ using the following scheme for $k = 1, 2, \ldots, N-1$ and $\forall\bar{\lambda} \in \mathbf{W}_h^E(\Omega_{\text{FEM}})$:

$$\begin{array}{l} \frac{1}{c^2}\left(\varepsilon_{rh}\frac{E_h^{k+1} - 2E_h^k + E_h^{k-1}}{\tau^2}, \bar{\lambda}\right) + (\nabla E_h^k, \nabla\bar{\lambda}) + \varepsilon_0(\nabla\cdot(\varepsilon_{rh}E_h^k), \nabla\cdot\bar{\lambda}) - (\nabla\cdot E_h^k, \nabla\cdot\bar{\lambda}) \\ +(g_h^k, \bar{\lambda})_{\partial\Omega_{\text{FEM}}} + \mu_0(\sigma_h \frac{E_h^{k+1} - E_h^{k-1}}{2\tau}, \bar{\lambda}) = 0, \\ {E_h}^0 = f_{0_h} \text{ and } {E_h}^1 = {E_h}^0 + \tau f_{1_h} \text{ in } \Omega_{\text{FEM}}. \end{array} \tag{22}$$

Rearranging the terms in (22), we obtain for $k = 1, 2, \ldots, N-1$ and $\forall\bar{\lambda} \in \mathbf{W}_h^E(\Omega_{\text{FEM}})$

$$\begin{array}{l} \left((1 + \tau c^2 \mu_0 \frac{\sigma_h}{2\varepsilon_{rh}})E_h^{k+1}, \bar{\lambda}\right) = \left(2E_h^k, \bar{\lambda}\right) - \left(E_h^{k-1}, \bar{\lambda}\right) - \tau^2 c^2 (1/\varepsilon_{rh}\nabla E_h^k, \nabla\bar{\lambda}) \\ - \tau^2 c^2 \varepsilon_0 (1/\varepsilon_{rh}\nabla\cdot(\varepsilon_{rh}E_h^k), \nabla\cdot\bar{\lambda}) + \tau^2 c^2 (1/\varepsilon_{rh}\nabla\cdot E_h^k, \nabla\cdot\bar{\lambda}) \\ + \tau^2 c^2 \left(\frac{g_h^k}{\varepsilon_{rh}}, \bar{\lambda}\right)_{\partial\Omega_{\text{FEM}}} + \tau c^2 \mu_0 (\frac{\sigma_h}{2\varepsilon_{rh}} E_h^{k-1}, \bar{\lambda}), \\ E_h^0 = f_{0_h} \text{ and } E_h^1 = E_h^0 + \tau f_{1_h} \text{ in } \Omega_{\text{FEM}}. \end{array} \tag{23}$$

The adjoint problem in Ω_{FEM} will be the following:

$$\begin{array}{ll} \frac{1}{c^2}\varepsilon_r \frac{\partial^2 \lambda}{\partial t^2} - \triangle\lambda - \varepsilon_0\varepsilon_r \nabla(\nabla\cdot\lambda) + \nabla(\nabla\cdot\lambda) - \mu_0\sigma\frac{\partial\lambda}{\partial t} = -(E - \widetilde{E})z_\delta \quad \text{for} & x \in S_T, \\ \lambda(\cdot,T) = \frac{\partial\lambda}{\partial t}(\cdot,T) = 0 \quad \text{for} & x \in \Omega_{\text{FEM}}, \\ \frac{\partial\lambda}{\partial n} = p \quad \text{on} \quad \partial\Omega_{\text{FEM}_T}. & \end{array} \tag{24}$$

The finite element method for the solution of adjoint problem (24) in Ω_{FEM} reads as follows: *Find* $\lambda_h \in \mathbf{W}_h^E(\Omega_{\text{FEM}})$ *such that* $\forall\bar{E} \in \mathbf{W}_h^E(\Omega_{\text{FEM}})$

$$\begin{array}{l} \frac{1}{c^2}\left(\varepsilon_{rh}\frac{\partial^2\lambda_h}{\partial t^2}, \bar{E}\right) + (\nabla\lambda_h, \nabla\bar{E}) + \varepsilon_0(\nabla\cdot\lambda_h, \nabla\cdot(\varepsilon_{rh}\bar{E})) - (\nabla\cdot\lambda_h, \nabla\cdot\bar{E}) \\ -(p_h, \bar{E})_{\partial\Omega_{\text{FEM}}} - \mu_0(\sigma_h\frac{\lambda_h}{t}, \bar{\lambda}) = -((E_h - \widetilde{E}_h)z_\delta, \bar{E}). \end{array} \tag{25}$$

Here, we define $E_h, \widetilde{E}_h, p_h$ to be the usual $\mathbf{W}_h^E$-interpolate of $E, \widetilde{E}, p$ in (24) in Ω_{FEM}.

We note that the adjoint problem should be solved backwards in time, from time $t = T$ to $t = 0$. To obtain the discrete scheme for (25), we approximate $\lambda_h(k\tau)$ by λ_h^k for $k = N, N-1, ..., 1$ using the following scheme for $k = N-1, \ldots, 1$:

$$\begin{aligned}&\frac{1}{c^2}\left(\varepsilon_{rh}\frac{\lambda_h^{k+1}-2\lambda_h^k+\lambda_h^{k-1}}{\tau^2}, \bar{E}\right) + (\nabla\lambda_h^k, \nabla\bar{E}) + \varepsilon_0(\nabla\cdot\lambda_h^k, \nabla\cdot(\varepsilon_{rh}\bar{E})) - (\nabla\cdot\lambda_h^k, \nabla\cdot\bar{E})\\ &-\left(p_h^k, \bar{E}\right)_{\partial\Omega_{\mathrm{FEM}}} - \mu_0(\sigma_h\frac{\lambda_h^{k+1}-\lambda_h^{k-1}}{2\tau}, \bar{E}) = -((E_h^k - \widetilde{E}_h^k)z_\delta, \bar{E}).\end{aligned} \tag{26}$$

Multiplying both sides of (26) by $\tau^2c^2/\varepsilon_{rh}$ and rearranging the terms, we obtain

$$\begin{aligned}&\left((1+\tau c^2\mu_0\frac{\sigma_h}{2\varepsilon_{rh}})\lambda_h^{k-1}, \bar{E}\right) = \left(2\lambda_h^k, \bar{E}\right) - \left(\lambda_h^{k+1}, \bar{E}\right) - \tau^2c^2(1/\varepsilon_{rh}\nabla\lambda_h^k, \nabla\bar{E})\\ &-\tau^2c^2\varepsilon_0(1/\varepsilon_{rh}\nabla\cdot\lambda_h^k, \nabla\cdot(\varepsilon_{rh}\bar{E})) + \tau^2c^2(1/\varepsilon_{rh}\nabla\cdot\lambda_h^k, \nabla\cdot\bar{E})\\ &+\tau^2c^2\left(\frac{p_h^k}{\varepsilon_{rh}}, \bar{E}\right)_{\partial\Omega_{\mathrm{FEM}}} + \tau c^2\mu_0(\frac{\sigma_h}{2\varepsilon_{rh}}\lambda_h^{k+1}, \bar{E}) - \tau^2c^2(1/\varepsilon_{rh}(E_h^k - \widetilde{E}_h^k)z_\delta, \bar{E}),\end{aligned} \tag{27}$$

for $k = N-1, \ldots, 1$, $\forall\bar{E} \in \mathbf{W}_h^E(\Omega_{\mathrm{FEM}})$

We note that, usually, $\dim U_h < \infty$ and $U_h \subset U^1$ as a set, and we consider U_h as a discrete analogue of the space U^1. We introduce the same norm in U_h as the one in U^0,

$$\|\bullet\|_{U_h} := \|\bullet\|_{U^0}, \tag{28}$$

where U_0 is defined in (9). From (28), it follows that all norms in finite dimensional spaces are equivalent. This allows us, in the numerical simulations of Section 5, to compute the discrete function ε_{rh}, which is an approximation of $\varepsilon_r(x)$, in the space C_h.

4.3. Fully Discrete Scheme in Ω_{FEM}

In this section, we present schemes for the computation of the solutions of forward (6) and adjoint (16) problems in Ω_{FEM}. After expanding functions $E_h(x)$ and $\lambda_h(x)$ in terms of the standard continuous piecewise linear functions $\{\varphi_i(x)\}_{i=1}^M$ in space as

$$E_h(x) = \sum_{i=1}^M E_{h_i}\varphi_i(x),\ \lambda_h(x) = \sum_{i=1}^M \lambda_{h_i}\varphi_i(x),$$

where E_{h_i} and λ_{h_i} denote unknown coefficients at the mesh point $x_i \in K_h, i = 1, ..., M$, we substitute them into (23) and (27), correspondingly, with $\bar{\lambda}(x,t) = \bar{E}(x,t) = \sum_{j=1}^M \varphi_j(x)$, and obtain the system of linear equations for the computation of the forward problem (6):

$$\begin{aligned}M_1E^{k+1} = 2ME^k - ME^{k-1} - \tau^2c^2G_1E^k - \tau^2c^2\varepsilon_0G_2E^k\\ + \tau^2c^2G_3E^k + \tau^2c^2F^k + \tau c^2\mu_0M_2E^{k-1}.\end{aligned} \tag{29}$$

Here, M, M_1, M_2 are the assembled block mass matrices in space; G_1, G_2, G_3 are the assembled block matrices in space; F^k is the assembled load vector at the time iteration k; E^k denotes the nodal values of $E_h(\cdot, t_k)$; τ is the time step. Now, we define the mapping F_K for the reference element $\hat{K}$ such that $F_K(\hat{K}) = K$ and let $\hat{\varphi}$ be the piecewise-linear local basis function on the reference element $\hat{K}$ such that $\varphi \circ F_K = \hat{\varphi}$. Then, the explicit formulas for the entries in the system of Equation (29) at each element K can be given as:

$$
\begin{aligned}
M_{i,j}^K &= (\varphi_i(x) \circ F_K, \varphi_j(x) \circ F_K)_K, \\
M1_{i,j}^K &= ((1 + \tau c^2 \mu_0 \frac{\sigma_h}{2\varepsilon_{r_h}})\varphi_i(x) \circ F_K, \varphi_j(x) \circ F_K)_K, \\
M2_{i,j}^K &= (\frac{\sigma_h}{2\varepsilon_{rh}}\varphi_i(x) \circ F_K, \varphi_j(x) \circ F_K)_K, \\
G1_{i,j}^K &= (\frac{1}{\varepsilon_{rh}}\nabla\varphi_i \circ F_K, \nabla\varphi_j \circ F_K)_K, \\
G2_{i,j}^K &= (\frac{1}{\varepsilon_{rh}}\nabla \cdot (\varepsilon_{rh}\varphi_i) \circ F_K, \nabla \cdot \varphi_j \circ F_K)_K, \\
G3_{i,j}^K &= (\frac{1}{\varepsilon_{r_h}}\nabla \cdot \varphi_i \circ F_K, \nabla \cdot \varphi_j \circ F_K)_K, \\
F_j^k &= (\frac{g_h^k}{\varepsilon_{r_h}}, \varphi_j \circ F_K)_{\partial K},
\end{aligned}
\tag{30}
$$

where $(\cdot,\cdot)_K$ denotes the $L_2(K)$ scalar product and ∂K is the part of the boundary of element K that lies at $\partial\Omega_{\text{FEM}}$.

For the case of adjoint problem (27), we obtain the system of linear equations:

$$
\begin{aligned}
M_1\lambda^{k-1} = {} & 2M\lambda^k - M\lambda^{k+1} - \tau^2c^2G_1\lambda^k - \tau^2c^2\varepsilon_0 G_2^T\lambda^k \\
& + \tau^2c^2G_3\lambda^k + \tau^2c^2P_1^k + \tau c^2\mu_0 M_2\lambda^{k+1} - \tau^2c^2P_2^k.
\end{aligned}
\tag{31}
$$

Here, $M, M_1, M_2, G_1, G_2, G_3$ are the assembled block matrices in space with explicit entries given in (30), and P_1^k, P_2^k are assembled load vectors at the time iteration k with explicit entries

$$
\begin{aligned}
P1_j^k &= (\frac{p_h^k}{\varepsilon_{rh}}, \varphi_j \circ F_K)_{\partial K}, \\
P2_j^k &= (1/\varepsilon_{rh}(E_h^k - \widetilde{E}_h^k)z_\delta, \varphi_j \circ F_K)_K,
\end{aligned}
\tag{32}
$$

λ^k denotes the nodal values of $\lambda_h(\cdot, t_k)$; τ is the time step.

Finally, for reconstructing $\varepsilon_r(x)$ in Ω_{IN}, we can use a gradient-based method with an appropriate initial guess value ε^0. The discrete versions in space of the gradients given in (15), after the integration by parts in space of the third term on the right-hand side of (15), have the form $\forall x \in \Omega_{\text{IN}}$:

$$
\begin{aligned}
g_h = {} & -\frac{1}{c^2}\lambda_h(x,0)f_{1_h} - \frac{1}{c^2}\int_0^T \frac{\partial\lambda_h}{\partial t}\frac{\partial E_h}{\partial t}\,dt \\
& + \varepsilon_0 \int_0^T (\nabla \cdot \lambda_h)(\nabla \cdot E_h)\,dt + \gamma(\varepsilon_{rh} - \varepsilon_h^0),
\end{aligned}
\tag{33}
$$

where ε_h^0 is the interpolant of ε^0. We note that because of the usage of the domain decomposition method, gradient (33) should be updated only in Ω_{IN} since, in Ω_{FDM} and in Ω_{OUT}, by condition (2), we have $\varepsilon_r = 1, \sigma = 0$. In (33), E_h and λ_h are the computed values of the forward and adjoint problems using schemes (29) and (31), correspondingly, and ε_{rh} is the approximate value of the computed relative dielectric permittivity function ε_r.

Finite Difference Formulation

We recall now that from condition (2), it follows that in Ω_{FDM}, the function $\varepsilon_r(x) = 1, \sigma = 0$. This means that in Ω_{FDM}, the model problem (6) transforms into the

following forward problem for an uncoupled system of acoustic wave equations for $E = (E_1, E_2, E_3)$:

$$\begin{array}{ll} \frac{\partial^2 E}{\partial t^2} - \Delta E = 0 & \text{in } \Omega_{\text{FDM}} \times (0,T), \\ E(\cdot,0) = f_0, \quad \frac{\partial E}{\partial t}(\cdot,0) = f_1 & \text{in } \Omega_{\text{FDM}}, \\ \frac{\partial E}{\partial n} = -\frac{\partial E}{\partial t} & \text{on } S_T, \\ \frac{\partial E}{\partial n} = \frac{\partial E_{\text{FEM}}}{\partial n} & \text{on } \partial\Omega^{\text{in}}_{\text{FDM}}, \end{array} \tag{34}$$

where $\frac{\partial E_{\text{FEM}}}{\partial n}$ are known values at $\partial\Omega^{\text{in}}_{\text{FDM}}$.

Using standard finite difference discretization of the first equation in (34) in Ω_{FDM}, we obtain the following explicit scheme for every component of the solution E of the forward problem (34):

$$E^{k+1}_{l,j,m} = \tau^2 \Delta E^k_{l,j,m} + 2E^k_{l,j,m} - E^{k-1}_{l,j,m}, \tag{35}$$

with correspondingly discretized boundary conditions. In the equations above, $E^k_{l,j,m}$ is the finite difference solution on the time iteration k at the discrete point (l,j,m), τ is the time step, and $\Delta E^k_{l,j,m}$ is the discrete Laplacian.

The adjoint problem in Ω_{FDM} will be:

$$\begin{array}{rl} \frac{\partial^2 \lambda}{\partial t^2} - \Delta\lambda = -(E - \widetilde{E}) z_\delta & \text{in } \Omega_{\text{FDM}} \times (0,T), \\ \lambda(\cdot,T) = \frac{\partial \lambda}{\partial t}(\cdot,T) = 0 & \text{in } \Omega_{\text{FDM}}, \\ \frac{\partial \lambda}{\partial n} = \frac{\partial \lambda}{\partial t} & \text{on } S_T, \\ \frac{\partial \lambda}{\partial n} = \frac{\partial \lambda_{\text{FEM}}}{\partial n} & \text{on } \partial\Omega^{\text{in}}_{\text{FDM}}, \end{array} \tag{36}$$

where $\frac{\partial \lambda_{\text{FEM}}}{\partial n}$ are known values at $\partial\Omega^{\text{in}}_{\text{FDM}}$.

Similarly to (37), we obtain the following explicit scheme for the solution of adjoint problem (36) in Ω_{FDM}, which we solve backwards in time:

$$\lambda^{k-1}_{l,j,m} = -\tau^2 (E - \widetilde{E})^k_{l,j,m} z_\delta + \tau^2 \Delta\lambda^k_{l,j,m} + 2\lambda^k_{l,j,m} - \lambda^{k+1}_{l,j,m}, \tag{37}$$

with corresponding discretized boundary conditions. In Equations (35) and (37), $(\cdot)^k_{l,j,m}$ is the solution on the time iteration k at the discrete point (l,j,m).

Note that we use FDM only inside Ω_{FDM}, and thus the computed values of $\frac{\partial E_{\text{FEM}}}{\partial n}$ and $\frac{\partial \lambda_{\text{FEM}}}{\partial n}$ can be approximated and will be known at $\partial\Omega^{\text{in}}_{\text{FDM}}$ through the finite element solution in Ω_{FEM}; see details in the domain decomposition Algorithm 2.

4.4. The Domain Decomposition Algorithm to Solve Forward and Adjoint Problems

First, we present the domain decomposition algorithm for the solution of state and adjoint problems. We note that, because of the use of the explicit finite difference scheme in Ω_{FDM}, we need to choose time step τ according to the CFL stability condition [38] such that the whole scheme remains stable.

Algorithm 2: The domain decomposition algorithm to solve forward and adjoint problems.

1: Construct the finite element mesh K_h in Ω_{FEM} and the finite difference mesh in Ω_{FDM}, as well as the time partition J_τ of the time interval $(0, T)$. At every time step k, we perform the following operations:
2: On the mesh in Ω_{FDM}, compute E^{k+1}, λ^{k-1} from (35), (37), correspondingly, using absorbing boundary conditions at the outer boundary $\partial\Omega$, with E^k, E^{k-1} and λ^k, λ^{k+1} known.
3: On the mesh K_h in Ω_{FEM}, compute E^{k+1}, λ^{k-1} using the finite element schemes (29) and (31), correspondingly, with E^k, E^{k-1} and λ^k, λ^{k+1} known.
4: Use the values of the functions E^{k+1}, λ^{k-1} at nodes ω_* overlapping with nodes $\omega_\diamond$, which are computed using the finite element schemes (29) and (31), correspondingly, as boundary conditions at the inner boundary $\partial\Omega^{\text{in}}_{\text{FDM}}$ for the finite difference method in Ω_{FDM}.
5: Use the values of the functions E^{k+1}, λ^{k-1} at nodes ω_{o} overlapping with nodes ω_+, which are computed using the finite difference schemes (35) and (37), correspondingly, as boundary conditions at $\partial\Omega_{\text{FEM}}$ for the finite element method in Ω_{FEM}.
6: Apply a swap of the solutions for the computed functions E^{k+1}, λ^{k-1}. Set $k = k + 1$ for the forward problem and $k = k - 1$ for the adjoint problem and go to step 2.

4.5. Reconstruction Algorithm for the Solution of Inverse Problem IP

We use the conjugate gradient method (CGM) for the iterative update of approximation ${\varepsilon_r}_h^m$ of the function ε_{rh}, where m is the number of iterations in the optimization algorithm. We introduce the following function

$$\begin{aligned} g_h^m(x) = &-\frac{1}{c^2}\lambda_h^m(x,0)f_{1h}(x) - \frac{1}{c^2}\int_0^T \frac{\partial\lambda_h^m}{\partial t}\frac{\partial E_h^m}{\partial t}\,dt \\ &+ \varepsilon_0 \int_0^T (\nabla\cdot\lambda_h^m)(\nabla\cdot E_h^m)\,dt + \gamma({\varepsilon_r}_h^m - \varepsilon_h^0), \end{aligned} \tag{38}$$

where functions E_h^m, λ_h^m are computed by solving the state and adjoint problems with $\varepsilon_r := {\varepsilon_r}_h^m, \sigma := \sigma_h^m$.

4.6. Adaptive Algorithms for Solution of the Inverse Problem IP

An adaptive algorithm allows the improvement of the already computed relative dielectric permittivity function ${\varepsilon_r}_h^M$ obtained on the initially non-refined mesh in the previous optimization algorithm (Algorithm 3). The idea of the local mesh refinement (note that we need it only in Ω_{IN}) is that it should be refined in all neighborhoods of all points in the mesh K_h where the function $|h\varepsilon_{rh}|$ achieves its maximum value, or where $|J'_{\varepsilon_r}(\varepsilon_{rh})|$ achieves its maximal values. These local mesh refinement recommendations are based on a posteriori error estimates for the error $|\varepsilon_r - \varepsilon_{rh}|$ in the reconstructed function ε_r (see the first mesh refinement indicator), and for the error $|J(\varepsilon_r) - J(\varepsilon_{rh})|$ in Tikhonov's functional (see the second mesh refinement indicator), respectively. The proofs of these a posteriori error estimates for arbitrary Tikhonov's functional are given in [19]. The a posteriori error for Tikhonov's functional (8) can be derived using the technique of [34], and it is a topic of ongoing research. Assuming that we have proof of these a posteriori error indicators, let us show how to compute them.

Algorithm 3: Conjugate gradient algorithm for determination of the relative dielectric permittivity function.

1: Initialize the mesh in Ω and the time partition J_τ of the time interval $(0,T)$. Start with the initial approximation $\varepsilon_{r_h}^0 = \varepsilon_h^0$ with known σ_h, and compute the sequence of $\varepsilon_{r_h}^m$ via the following steps:
2: Compute solutions $E_h(x,t,\varepsilon_{r_h}^m,\sigma_h)$ and $\lambda_h\left(x,t,\varepsilon_{r_h}^m,\sigma_h\right)$ of the forward and adjoint problems on K_h and J_τ using the domain decomposition algorithm (Algorithm 2).
3: Update the function $\varepsilon_{rh} := \varepsilon_{r_h}^{m+1}$ on K_h and J_τ using the CGM as

$$\varepsilon_{r_h}^{m+1} = \varepsilon_{r_h}^{m} + \alpha d^m(x),$$

where α is the step size in the gradient update [39] and

$$d^m(x) = -g_h^m(x) + \beta^m d^{m-1}(x),$$

with

$$\beta^m = \frac{\|g_h^m(x)\|^2}{\|g_h^{m-1}(x)\|^2},$$

Here, $d^0(x) = -g_h^0(x)$.
4: Stop computing $\varepsilon_{r_h}^m$ at the iteration $M := m$ and obtain the function $\varepsilon_{r_h}^M := \varepsilon_{hr}{}^m$ if either $\|g_h^m\|_{L_2(\Omega)} \le \theta$ or norms $\|\varepsilon_{r_h}^m\|_{L_2(\Omega)}$ are stabilized. Here, θ is the tolerance chosen by the user. Otherwise, set $m := m+1$ and go to step 2.

We define by $E(\varepsilon_r,\sigma), \lambda(\varepsilon_r,\sigma)$ the exact solutions of the forward and adjoint problems for exact ε_r, σ, respectively. Then, by defining

$$u(\varepsilon_r,\sigma) = (E(\varepsilon_r,\sigma), \lambda(\varepsilon_r,\sigma), \varepsilon_r) \in U^1,$$

and using the fact that, for exact solutions $E(\varepsilon_r,\sigma), \lambda(\varepsilon_r,\sigma)$, we have

$$J(E(\varepsilon_r,\sigma),\varepsilon_r) = L(u(\varepsilon_r,\sigma)). \tag{39}$$

Assuming now that solutions $E(\varepsilon_r,\sigma), \lambda(\varepsilon_r,\sigma)$ are sufficiently stable, we can write that the Frechét derivative of the Tikhonov functional is the following function:

$$J'_{\varepsilon_r}(\varepsilon_r,\sigma) = \frac{\partial J}{\partial \varepsilon_r}(E(\varepsilon_r,\sigma),\varepsilon_r) = \frac{\partial L}{\partial \varepsilon_r}(u(\varepsilon_r,\sigma)). \tag{40}$$

Inserting (15) into (40), we obtain

$$\begin{aligned} J'_{\varepsilon_r}(\varepsilon_r,\sigma) = &-\frac{1}{c^2}\lambda(x,0)f_1(x) - \frac{1}{c^2}\int_0^T \frac{\partial \lambda}{\partial t}\frac{\partial E}{\partial t}\,dt \\ &- \varepsilon_0 \int_0^T E\nabla(\nabla\cdot\lambda)\,dt + \gamma(\varepsilon_r - \varepsilon^0)(x). \end{aligned} \tag{41}$$

In the second mesh refinement indicator, a discretized version of (41) is used, computed for approximations $(\varepsilon_{rh}, \sigma_h)$.

- The First Mesh Refinement Indicator
  Refine the mesh in the neighborhoods of those points of K_h where the function $|h\varepsilon_{rh}|$ attains its maximal values. In other words, refine the mesh in such subdomains of K_h where

$$|h\varepsilon_{rh}| \ge \widetilde{\beta} \max_{K_h} |h\varepsilon_{rh}|.$$

Here, $\widetilde{\beta} \in (0,1)$ is a number that should be chosen computationally and h is the mesh function (17) of the finite element mesh K_h.

- The Second Mesh Refinement Indicator
  Refine the mesh in the neighborhoods of those points of K_h where the function $|J'_{\varepsilon_r}(E, \varepsilon_{rh})|$ attains its maximal values. More precisely, let $\beta \in (0,1)$ be the tolerance number, which should be chosen in computational experiments. Refine the mesh K_h in such subdomains where

$$|J'_{\varepsilon_r}(E, \varepsilon_{rh})| \geq \beta \max_{K_h} |J'_{\varepsilon_r}(E, \varepsilon_{rh})|. \tag{42}$$

Algorithm 4: Adaptive Algorithm, first version.

1: Construct the finite difference mesh in Ω_{FDM}. Choose an initial space–time mesh $K_{h0} \times J_{\tau_0}$ in $\Omega_{\text{FEM}} \times [0,T]$. Compute the sequence of $\varepsilon_{rk}, k > 0$, via the following steps:
2: Obtain numerical solution ε_{rk} with known function σ_k on K_{h_k} using Algorithm 3 (Conjugate Gradient Method).
3: Refine such elements in the mesh K_{h_k} where the first mesh refinement indicator

$$|h\varepsilon_{rk}| \geq \widetilde{\beta}_k \max_{K_{hk}} |h\varepsilon_{rk}| \tag{43}$$

is satisfied. Here, the tolerance numbers $\widetilde{\beta}_k \in (0,1)$ are chosen by the user.
4: Define a new refined mesh as $K_{h_{k+1}}$ and construct a new time partition $J_{\tau_{k+1}}$ such that the CFL condition is satisfied. Interpolate $\varepsilon_{rk}, \sigma_k$ on a new mesh $K_{h_{k+1}}$ and perform steps 2–4 on the space–time mesh $K_{h_{k+1}} \times J_{\tau_{k+1}}$. Stop mesh refinements when $||\varepsilon_{rk} - \varepsilon_{rk-1}|| < tol_1$ or $||g_h^k(x)|| < tol_2$, where $tol_i, i = 1,2$ are tolerances chosen by the user.

Algorithm 5: Adaptive Algorithm, second version.

1: Choose an initial space–time mesh $K_{h_0} \times J_{\tau_0}$ in Ω_{FEM}. Compute the sequence $\varepsilon_{rk}, k > 0$ with known σ_k, on refined meshes K_{h_k}, via the following steps:
2: Obtain numerical solutions ε_{rk} on $K_{h_k} \times J_{\tau_k}$ using Algorithm 3 (Conjugate Gradient Method).
3: Refine the mesh K_{h_k} at all points where the second mesh refinement indicator

$$|g_h^k(x)| \geq \beta_k \max_{K_{hk}} |g_h^k(x)|, \tag{44}$$

is satisfied. Here, indicator g_h^k is defined in (38). Tolerance number $\beta_k \in (0,1)$ should be chosen in numerical examples.
4: Define a new refined mesh as $K_{h_{k+1}}$ and construct a new time partition $J_{\tau_{k+1}}$ such that the CFL condition is satisfied. Interpolate $\varepsilon_{rk}, \sigma_k$ on a new mesh $K_{h_{k+1}}$ and perform steps 1–3 on the space–time mesh $K_{h_{k+1}} \times J_{\tau_{k+1}}$. Stop mesh refinements when $||\varepsilon_{rk} - \varepsilon_{rk-1}|| < tol_1$, or $||g_h^k(x)|| < tol_2$, where $tol_i, i = 1,2$ are tolerances chosen by the user.

Remark 1.

1. *We note that in (42), exact values of $E(x,t), \lambda(x,t)$ are used, obtained with the already computed functions $(\varepsilon_{rh}, \sigma_h)$; see (41). However, in our algorithms and in computations, we approximate the exact values of $E(x,t), \lambda(x,t)$ by the computed ones $E_h(x,t), \lambda_h(x,t)$.*
2. *In both mesh refinement indicators, we use the fact that functions ε_r, σ are unknown only in Ω_{IN}.*

We define the minimizer of the Tikhonov functional (8) and its approximated finite element solution on a k-times adaptively refined mesh K_{h_k} by ε_r and ε_{rk}, correspondingly. In both of our mesh refinement recommendations, we need to compute the functions ε_{rk} on the mesh K_{h_k}. To do this, we apply Algorithm 3 (conjugate gradient algorithm). We will define by $\varepsilon_{rk} := \varepsilon_{r_h}^M$ values obtained at step 3 of the conjugate gradient algorithm.

Remark 2.

1. *First, we describe how to choose the tolerance numbers $\widetilde{\beta}_k, \beta_k$ in (43) and (44). Their values depend on the concrete values of $\max_{\Omega_{IN}} |h\varepsilon_{rk}|$ and $\max_{\Omega_{IN}} |g_h^k(x)|$, correspondingly. If we take values of $\beta_k, \widetilde{\beta}_k$ that are very close to 1, then we will refine the mesh in a very narrow region of the Ω_{IN}, and if we choose $\beta_k, \widetilde{\beta}_k \approx 0$, then almost all elements in the finite element mesh will be refined, and, thus, we will obtain global and not local mesh refinement.*
2. *To compute L_2 norms $||\varepsilon_{rk} - \varepsilon_{rk-1}||$, in step 3 of the adaptive algorithms, the reconstruction ε_{rk-1} is interpolated from the mesh $K_{h_{k-1}}$ to the mesh K_{h_k}.*
3. *The computational mesh is refined only in Ω_{FEM} such that no new nodes are added in the overlapping elements between two domains, Ω_{FEM} and Ω_{FDM}. Thus, the mesh in Ω_{FDM}, where the finite difference method is used, always remains unchanged.*

5. Numerical Examples

In this section, we present numerical simulations of the reconstruction of the permittivity function of a three-dimensional anatomically realistic breast phantom taken from an online repository [1] using the adaptive reconstruction Algorithm 4 of Section 4.6. We have tested the performance of the adaptive Algorithm 5 and it is slightly more computationally expensive in terms of time compared to the performance of Algorithm 4. Additionally, relative errors in the reconstructions of the dielectric permittivity function are slightly smaller for Algorithm 4 and, thus, in this section, we present the results of reconstruction for Algorithm 4.

5.1. Description of Anatomically Realistic Data

We have tested our reconstruction algorithm using a three-dimensional realistic breast phantom with ID = 012204 provided in the online repository [1]. The phantom comprises the structural heterogeneity of normal breast tissue for the realistic dispersive properties of normal breast tissue at 6 GHz reported in [40,41]. The breast phantoms of database [1] are derived using T1-weighted MRIs of patients in prone position. Every phantom presents a 3D mesh of cubic voxels of the size $0.5 \times 0.5 \times 0.5$ mm.

Tissue types and corresponding media numbers of breast phantoms are taken from [1] and are given in Table 1. The spatial distribution of these media numbers for the phantom with ID = 012204 is presented in Figure 3a–c.

The figures demonstrate the distribution of media numbers on the original coarse mesh consisting of 34,036,992 nodes. Clearly, performing computations on a such large mesh is a computationally demanding task, and thus, we have sampled the original mesh. In all our computations, we have used the mesh consisting of 63,492 nodes as a coarse finite element mesh, which was obtained by taking every 8th node in x_1, x_2 and x_3 directions of the original mesh. Figures 4 and 5 show the spatial distribution of dielectric permittivity ε_r and effective conductivity σ (S/m) on original and sampled meshes.

Figure 3d demonstrates the distribution of media numbers on the finally sampled mesh. Figure 6 presents the spatial distribution of weighted values of ε_r on the original and finally sampled mesh for Test 1. The testing of our algorithms on other sampled meshes is a computationally expensive task, requiring the running of programs in parallel infrastructure, and can be considered as a topic for future research.

We note that in all our computations, we scaled the original values of ε_r and σ of database [1] presented in Figures 4 and 5 and considered weighted versions of these parameters, in order to satisfy condition (2), as well as for the efficient implementation

of FE/FD DDM for the solution of forward and adjoint problems. Table 1 presents the weighted values of ε_r and σ used in the numerical tests of this section. Thus, in this way, we obtained a computational set-up corresponding to the domain decomposition method that was used in Algorithms 2–5.

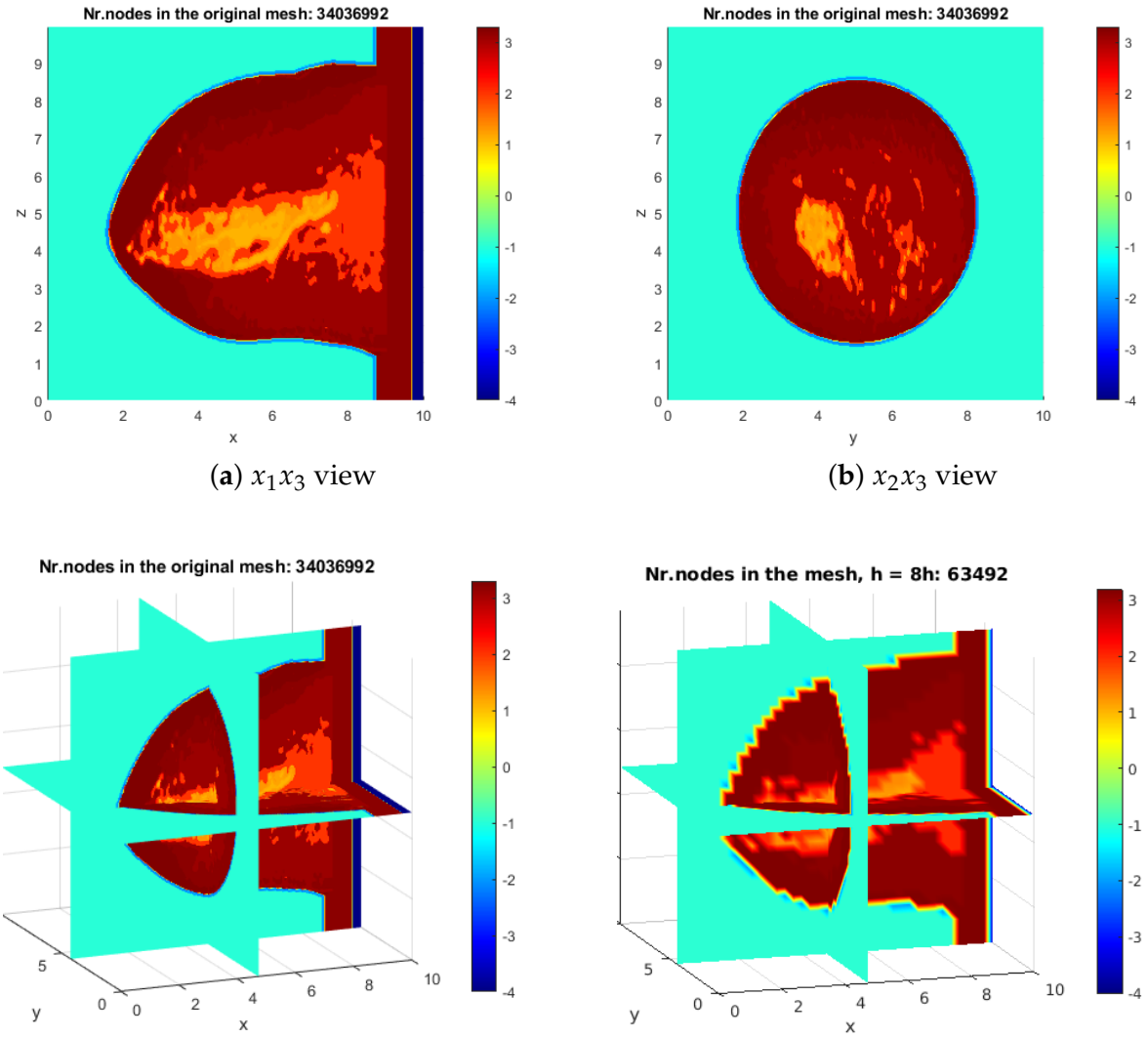

(**a**) x_1x_3 view (**b**) x_2x_3 view

(**c**) prospect view (**d**) prospect view

Figure 3. (**a**–**c**) Original values and (**d**) sampled values of the spatial distribution of media numbers of Table 1 for breast phantom of object *ID*_012204 of database [1]. Figures are produced by MATLAB code provided at [42]. Table 1 clarifies the description of media numbers and corresponding tissue types.

Table 1. Tissue types and corresponding media numbers of database [1] together with realistic weighted values of ε_r and σ (S/m) for breast phantom with ID = 012204 used in numerical experiments of Section 5.2. Figure 3 presents media numbers of this table on original and sampled meshes.

Tissue Type	Media Number	Test 1 $\varepsilon_r/5$	Test 1 $\sigma/5$	Test 2 $\varepsilon_r/5$	Test 2 $\sigma/5$
Immersion medium	-1	1	0	1	0
Skin	-2	1	0	1	0
Muscle	-4	1	0	1	0
Fibroconnective/glandular-1	1.1	9	1.2	9	1.2
Fibroconnective/glandular-2	1.2	8	1	1	0
Fibroconnective/glandular-3	1.3	8	1	1	0
Transitional	2	1	0	1	0
Fatty-1	3.1	1	0	1	0
Fatty-2	3.2	1	0	1	0
Fatty-3	3.3	1	0	1	0

5.2. Computational Set-Up

We have used the domain decomposition Algorithm 2 of Section 4.4 to solve forward and adjoint problems in the adaptive reconstruction Algorithm 4. To do this, we set the dimensionless computational domain Ω as

$$\Omega = \{x = (x_1, x_2, x_3) \in (-0.8840, 0.8824) \times (-0.8630, 0.8648) \times (-0.8945, 0.8949)\},$$

and the domain Ω_{FEM} as

$$\Omega_{\text{FEM}} = \{x = (x_1, x_2, x_3) \in (-0.7, 0.6984) \times (-0.7, 0.7018) \times (-0.7, 0.7004)\}.$$

We choose the coarse mesh sizes $h_1 = 0.0368, h_2 = 0.0326, h_3 = 0.0389$ in x_1, x_2, x_3 directions, respectively, in $\Omega = \Omega_{\text{FEM}} \cup \Omega_{\text{FDM}}$, as well as in the overlapping regions between Ω_{FEM} and Ω_{FDM}. Corresponding physical domains in meters are $\tilde{\Omega} = 0.17664 \times 0.17278 \times 0.17894$ m for Ω and $\tilde{\Omega}_{\text{FEM}} = 0.13985 \times 0.14018 \times 0.14004$ m for Ω_{FEM}.

The boundary $\partial\Omega$ of the domain Ω is decomposed into three different parts such that $\partial\Omega = \partial_1\Omega \cup \partial_2\Omega \cup \partial_3\Omega$, where $\partial_1\Omega$ and $\partial_2\Omega$ are, respectively, the front and back sides of Ω, and $\partial_3\Omega$ is the union of the left, right, top and bottom sides of this domain. We collect time-dependent observations at $\Gamma_2 := \partial_2\Omega \times (0, T)$, or at the transmitted side $\partial_2\Omega$ of Ω. We also define $\Gamma_{1,1} := \partial_1\Omega \times (0, t_1]$, $\Gamma_{1,2} := \partial_1\Omega \times (t_1, T)$, and $\Gamma_3 := \partial_3\Omega \times (0, T)$.

The following model problem was used in all computations:

$$\begin{aligned} \frac{1}{c^2}\varepsilon_r \frac{\partial^2 E}{\partial t^2} + \nabla(\nabla \cdot E) - \triangle E - \varepsilon_0 \nabla(\nabla \cdot (\varepsilon_r E)) &= -\mu_0 \sigma \frac{\partial E}{\partial t} \text{ in } \Omega_T, \\ E(x,0) = 0, \quad \frac{\partial E}{\partial t}(x,0) &= 0 \text{ in } \Omega, \\ \frac{\partial E}{\partial n} &= f(t) \text{ on } \Gamma_{1,1}, \\ \frac{\partial E}{\partial n} &= -\frac{\partial E}{\partial t} \text{ on } \Gamma_{1,2} \cup \Gamma_2, \\ \frac{\partial E}{\partial n} &= 0 \text{ on } \Gamma_3. \end{aligned} \tag{45}$$

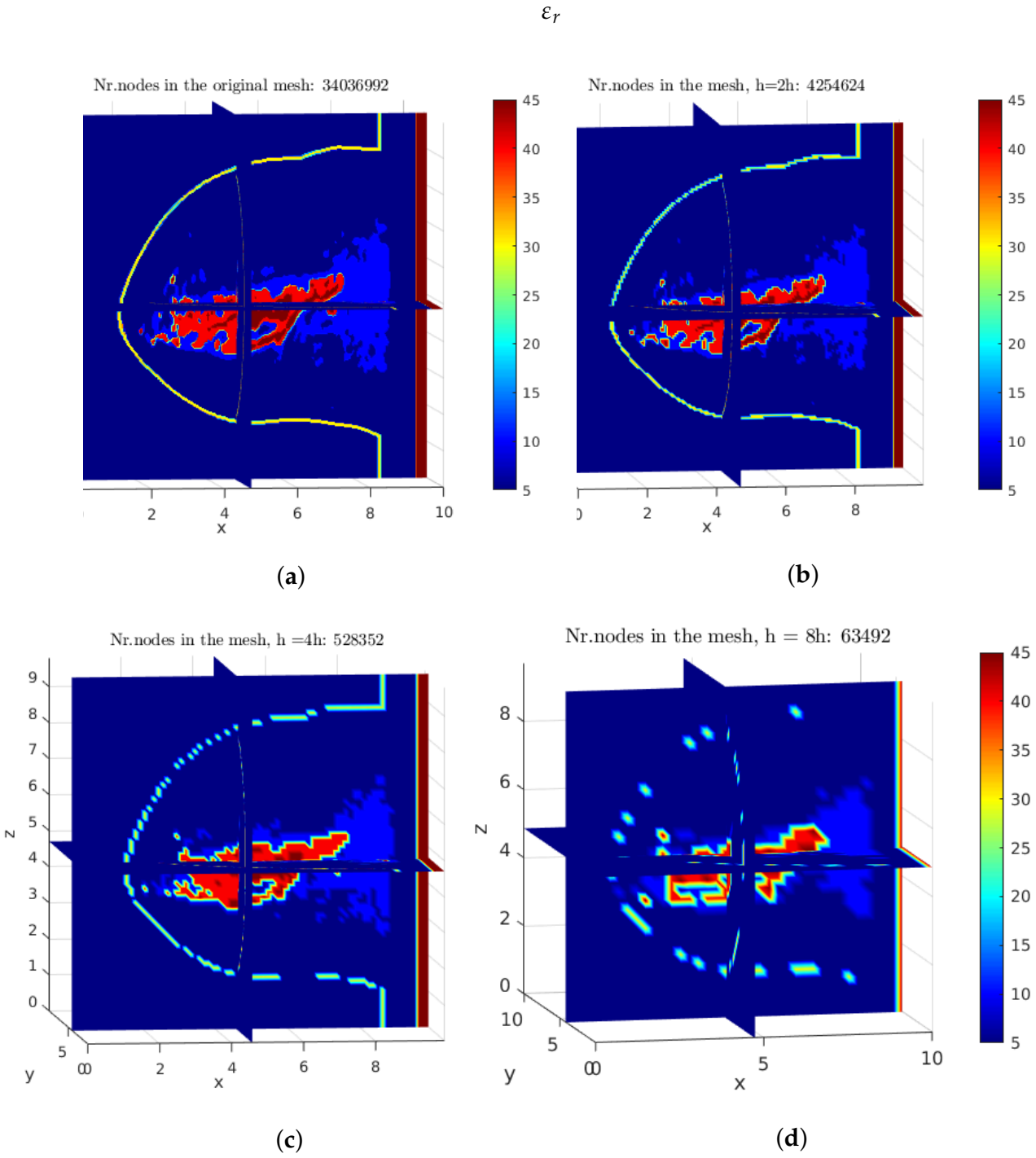

Figure 4. Spatial distribution of realistic ultrawideband dielectric properties of 3D breast phantom of database [1] developed at the Department of Electrical and Computer Engineering at the University of Wisconsin-Madison, USA. (**a**) shows original values of ε_r at 6 GHz for object ID_012204 of database [1]. (**b**–**d**) present sampled versions of ε_r. Figures are produced by MATLAB code provided at [42].

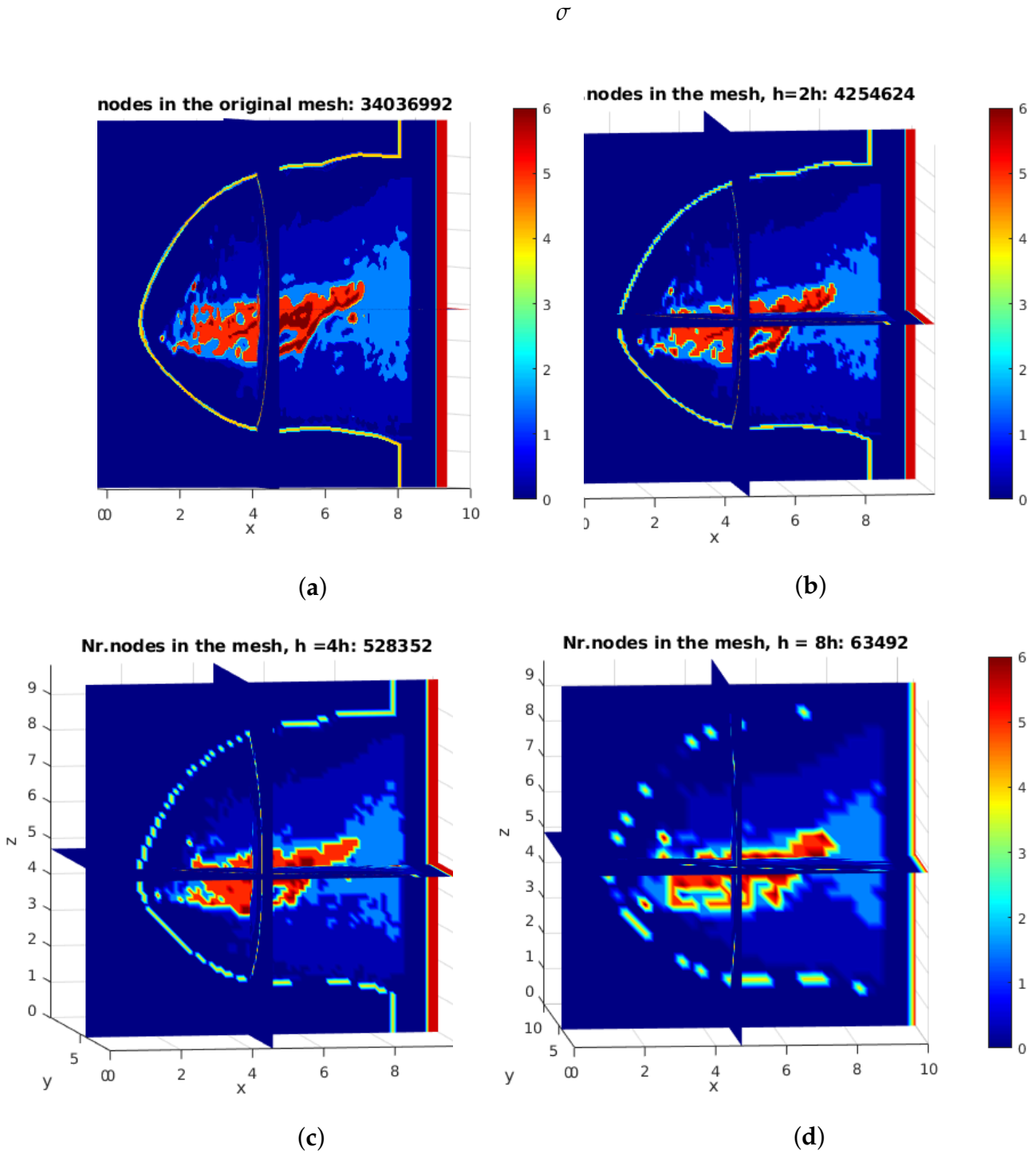

Figure 5. Spatial distribution of realistic ultrawideband dielectric properties of 3D breast phantom of database [1] developed at the Department of Electrical and Computer Engineering at the University of Wisconsin-Madison, USA. (**a**) shows original values of σ (S/m) at 6 GHz for object *ID*_012204 of database [1]. (**b**–**d**) present sampled versions of σ (S/m). Figures are produced by MATLAB code provided at [42].

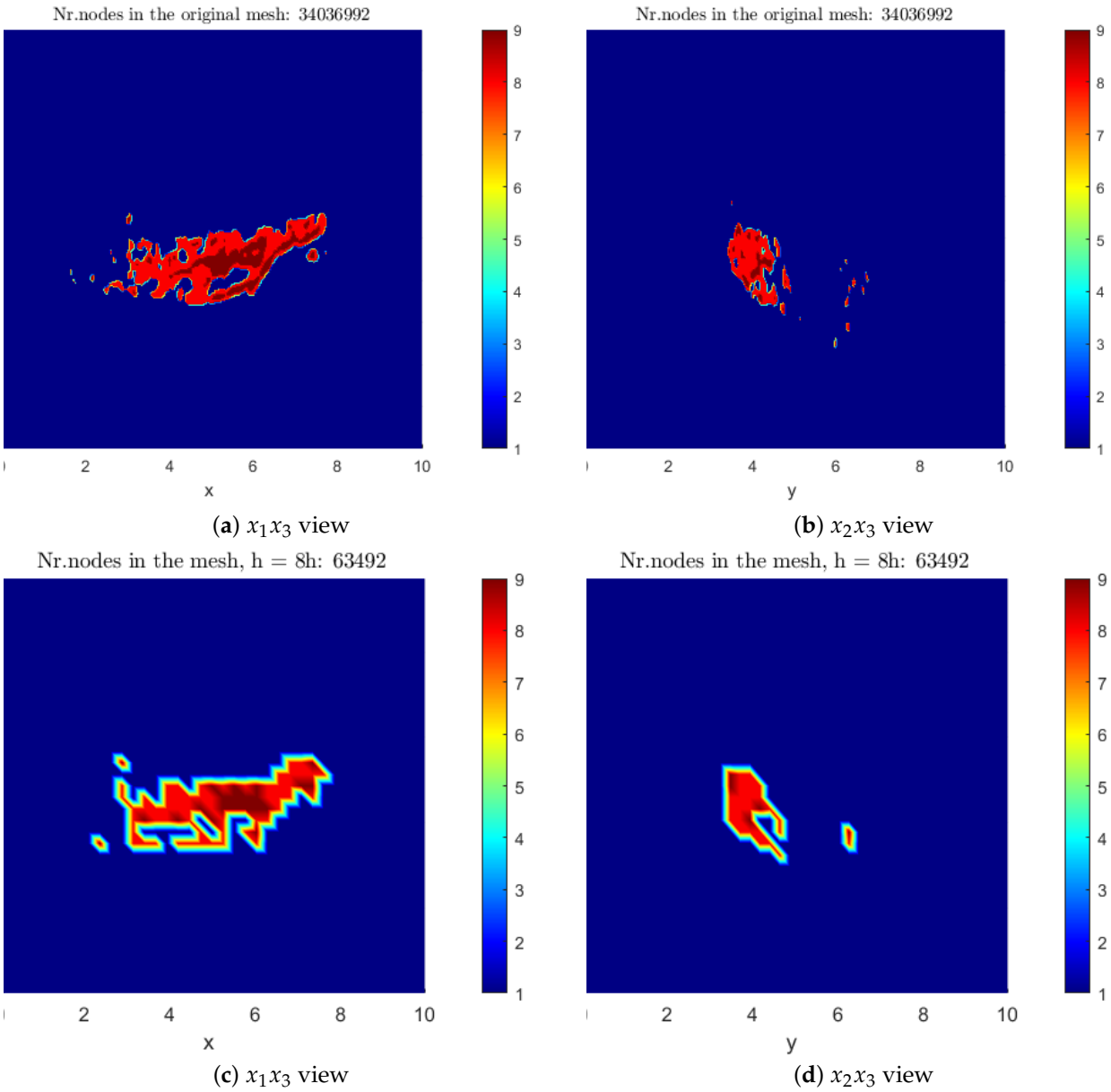

(**a**) x_1x_3 view (**b**) x_2x_3 view

(**c**) x_1x_3 view (**d**) x_2x_3 view

Figure 6. Test 1. Slices of weighted exact ε_r; see Table 1 for description of different tissue types and values of weighted ε_r. (**a**,**b**) Slices on original mesh with mesh size h. (**c**,**d**) Slices on sampled mesh with mesh size 8 h.

We initialize a plane wave $f(t) = (0, f_2, 0)(t)$ for one component E_2 of the electric field $E = (E_1, E_2, E_3)$ at $\Gamma_{1,1}$ in (45). The function $f_2(t)$ represents the single direction of a plane wave that is initialized at $\partial_1\Omega$ in time $t = [0, 3.0]$ and is defined as

$$f_2(t) = \begin{cases} \sin(\omega t), & \text{if } t \in \left(0, \frac{2\pi}{\omega}\right), \\ 0, & \text{if } t > \frac{2\pi}{\omega}. \end{cases} \tag{46}$$

The goal of our numerical tests in Test 1 and Test 2 was to reconstruct the weighted dielectric permittivity function ε_r shown in Figure 7a,b. Figures 8a–c and 9a–c present simulated solution $|E_h|$ in Ω_{FEM} of model problem (45) for Test 1 and Test 2, correspondingly.

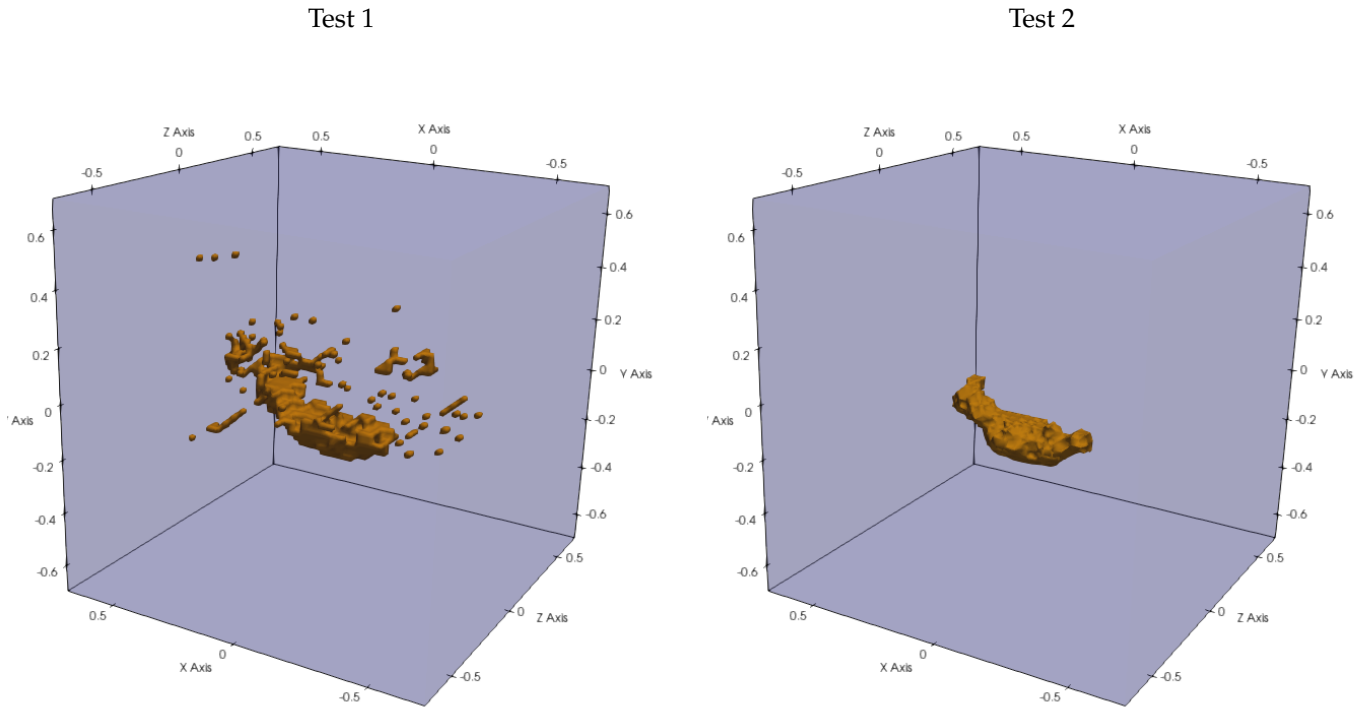

Figure 7. Isosurface of weighted exact dielectric permittivity with value $\varepsilon_r \approx 5$ corresponding to tissue type "fibroconnective/glandular-1" (**a**) in Test 1 and (**b**) in Test 2. Table 1 clarifies the description of different tissue types.

To perform computations for the solution of the inverse problem, we add normally distributed Gaussian noise with mean $\mu = 0$ to the simulated electric field at the transmitted boundary $\partial_2\Omega$. Then, we smooth out these data in order to obtain reasonable reconstructions; see the details of the data preprocessing in [17,18]. Computations of forward and inverse problems were performed in time $T = [0, 3]$ with equidistant time step $\tau = 0.006$, satisfying the CFL condition. Thus, it took 500 time steps at every iteration of reconstruction Algorithm 4 to solve the forward or adjoint problem. The time interval $T = [0, 3]$ was chosen computationally such that the initialized plane wave could reach the transmitted boundary $\partial_2\Omega$ in order to obtain meaningful reflections from the object inside the domain Ω_{FEM}. Figures 8a–c, 9a–c and 10a–i show these reflections in different tests. Experimentally, such signals can be produced by a Picosecond Pulse Generator connected with a horn antenna, and scattered time-dependent signals can be measured by a Tektronix real-time oscilloscope; see [17,18] for details of the experimental set-up for the generation of a plane wave and collecting time-dependent data. For example, in our computational set-up, the experimental time step between two signals can be $\tilde{\tau} = 6$ picoseconds and every signal should be recorded during $\tilde{T} = 3$ nanoseconds.

We have chosen the following set of admissible parameters for reconstructed function $\varepsilon_r(x)$

$$M_{\varepsilon_r} = \{\rho \in C^2(\overline{\Omega}) | 1 \leq \varepsilon_r(x) \leq 10\}, \tag{47}$$

as well as tolerance $\theta = 10^{-5}$ at step 3 of the conjugate gradient Algorithm 3. Parameter β_k in the refined procedure of Algorithm 4 was chosen as the constant $\beta_k = 0.8$ for all refined meshes K_{hk}.

Figures 8d–i and 9d–i show simulated data of model problem (45) for all components $(E_1, E_2, E_3)(x, t)$ of electric field $E(x, t)$ at different times at the transmitted boundary $\partial_2\Omega$. Figures 8d–f and 9d–f show randomly distributed noisy data and Figures 8g–i and 9g–i show smoothed noisy data used for the solution of the inverse problem.

These figures show that the largest amplitude reflections, or transmitted data, are obtained from the second component E_2 of the electric field E. The same observation was obtained in previous works [34,35], where the authors used a similar computational set-up with a plane wave. However, a comparison of all three components was not presented in [34]. The domination of reflections at the transmitted boundary from the E_2 component can be explained by the fact that we initialized only one component of the electric field $E = (E_1, E_2, E_3)$ as a plane wave $f(t) = (0, f_2, 0)(t)$ at $\Gamma_{1,1}$ in the model problem (45), and thus two other components E_1, E_3 will be smaller by amplitude than the E_2 when we use the explicit scheme (29) for computations. See also the theoretical justification of this fact in [43].

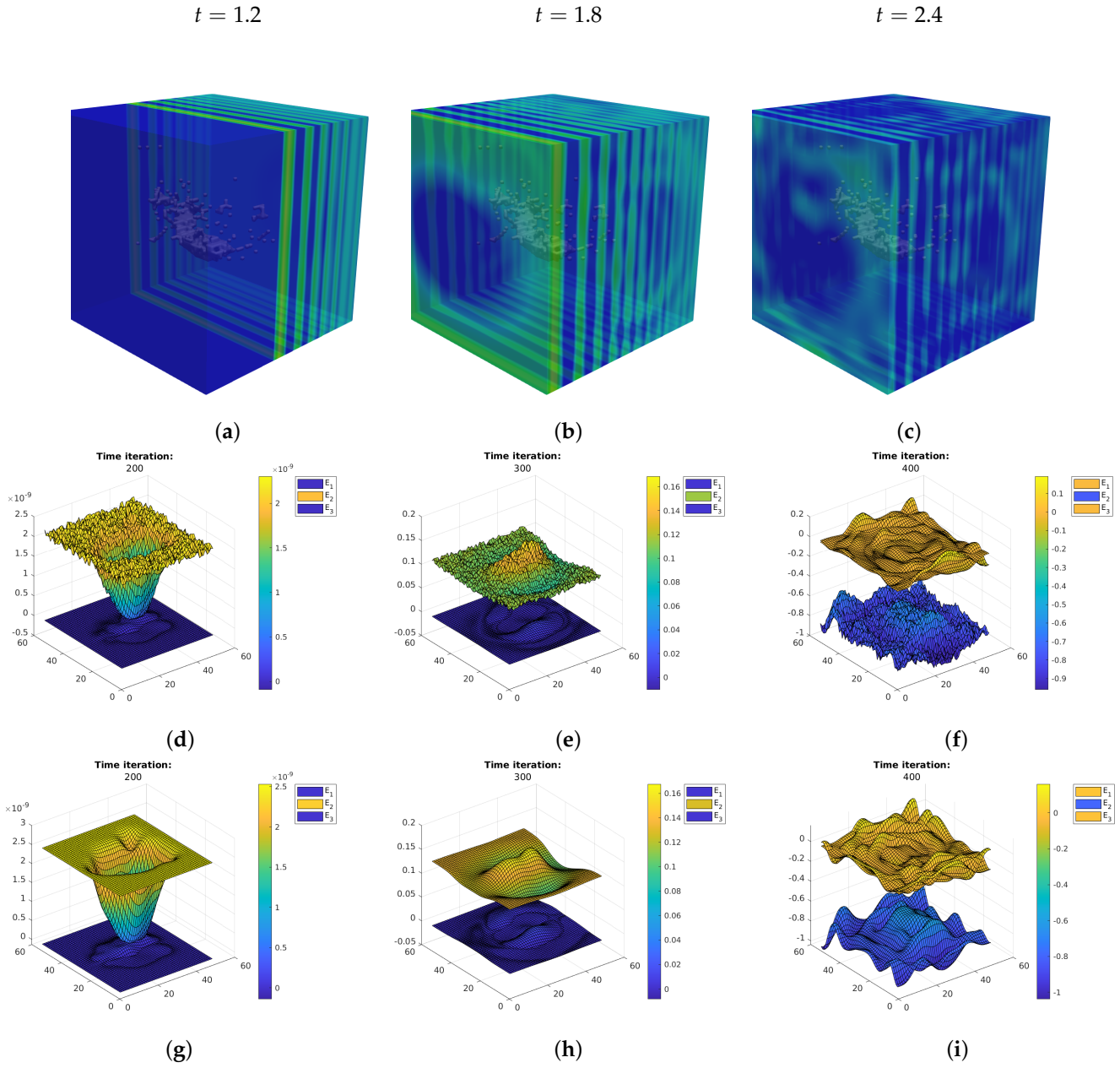

Figure 8. Test 1. (**a**–**c**): Solution $|E_h|$ of model problem (45) at different times for $\omega = 40$ in (46). (**d**–**f**): Transmitted noisy scattered data $E_h = (E_{1h}, E_{2h}, E_{3h})$ of components of electric field $E = (E_1, E_2, E_3)$ at different times. (**g**–**i**): Smoothed transmitted scattered data $E_h = (E_{1h}, E_{2h}, E_{3h})$ of components of electric field $E = (E_1, E_2, E_3)$ at different times. The noise level in data is $\delta = 10\%$.

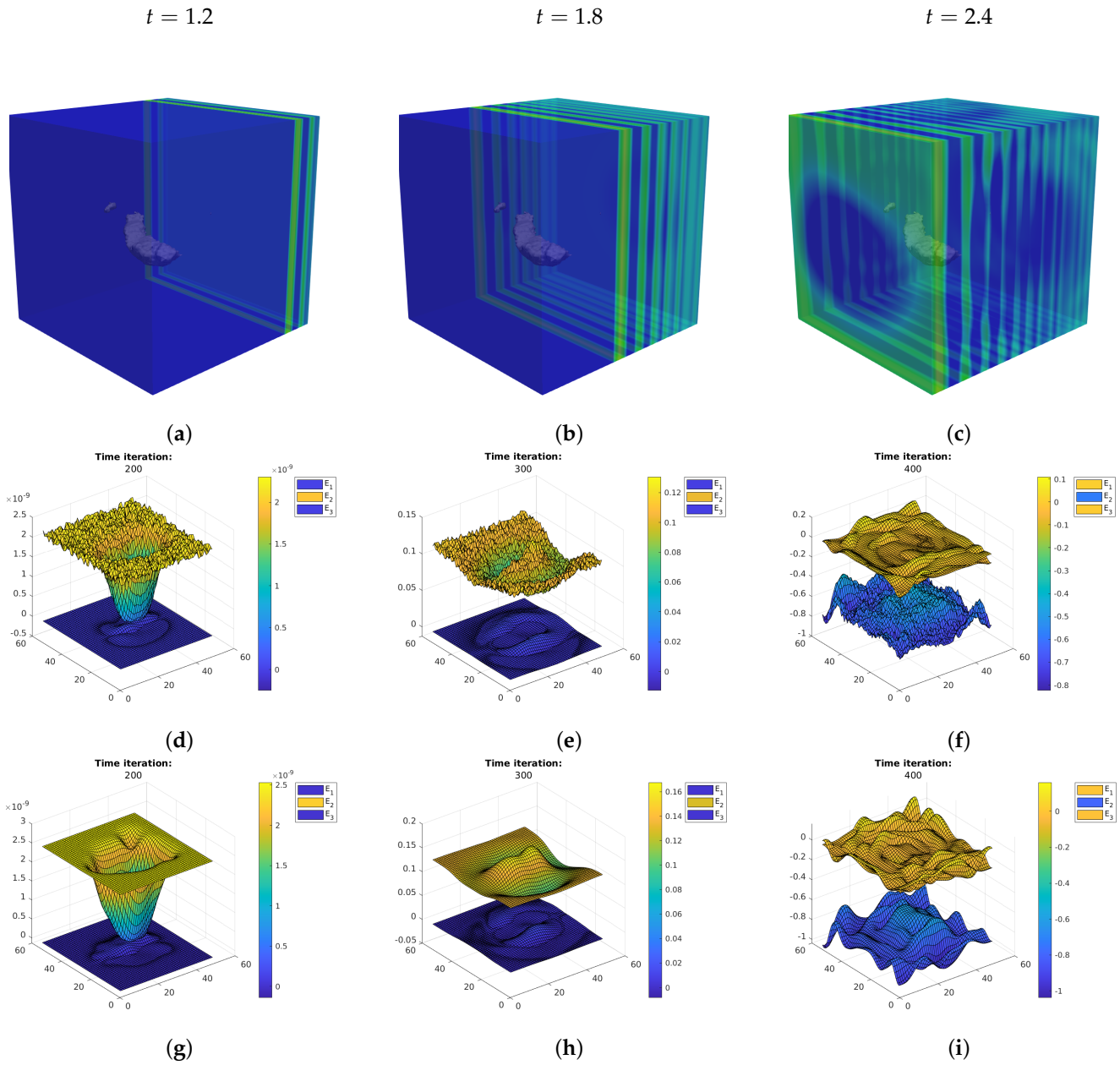

Figure 9. Test 2. (**a**–**c**): Solution $|E_h|$ of model problem (45) at different times for $\omega = 40$ in (46). (**d**–**f**): Transmitted noisy scattered data $E_h = (E_{1h}, E_{2h}, E_{3h})$ of components of electric field $E = (E_1, E_2, E_3)$ at different times. (**g**–**i**): Smoothed transmitted scattered data $E_h = (E_{1h}, E_{2h}, E_{3h})$ of components of electric field $E = (E_1, E_2, E_3)$ at different times. The noise level in data is $\delta = 10\%$.

The numerical tests of [34] show that the best reconstruction results of the space-dependent function $\varepsilon_r(x)$ for $\sigma = 0$ in Ω are obtained for $\omega = 40$ in (46). Thus, we performed simulations of the forward problem (45) taking $\sigma = 0$ for different $\omega = 40, 60, 80, 100$ in (46). We found that, for the chosen computational set-up with final time $T = 3$, maximal values of scattered function E_2 were obtained for $\omega = 40$. Thus, we take $\omega = 40$ in (46) in all our tests.

We assume that both functions ε_r, σ satisfy condition (2): they are known inside $\Omega_{\text{out}} \cup \Omega_{\text{FDM}}$ and unknown inside Ω_{IN}. The goal of our numerical tests is to reconstruct the function ε_r of the domain Ω_{FEM} of Figure 7 under condition (2) and the additional condition that the function $\sigma(x)$ of this domain is known. See Table 1 for the distribution of ε_r, σ in Ω_{FEM}.

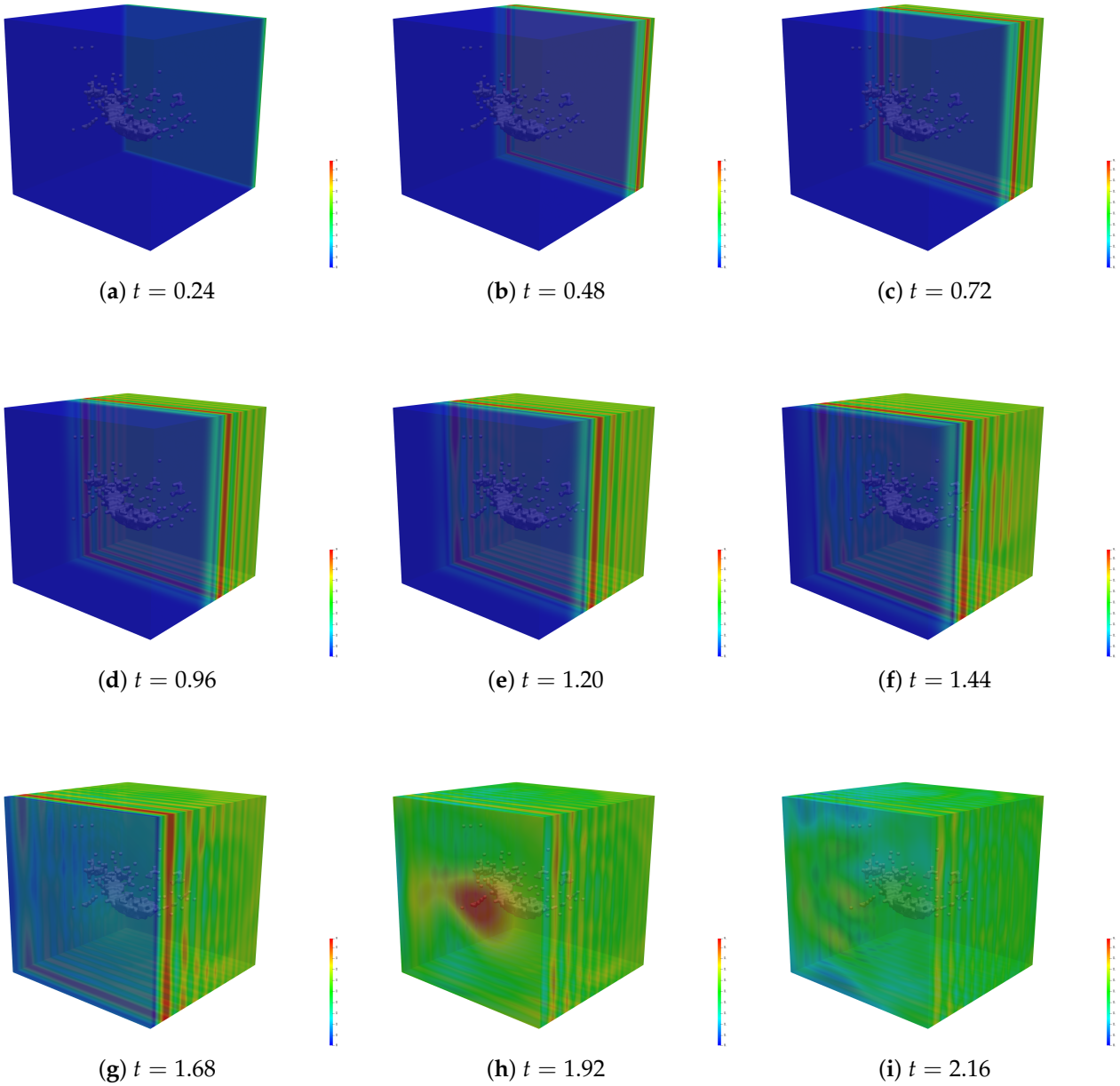

(**a**) $t = 0.24$ (**b**) $t = 0.48$ (**c**) $t = 0.72$

(**d**) $t = 0.96$ (**e**) $t = 1.20$ (**f**) $t = 1.44$

(**g**) $t = 1.68$ (**h**) $t = 1.92$ (**i**) $t = 2.16$

Figure 10. The figures (**a–i**) illustrate how our planar wave f used in implementations propagates through the medium by color plotting $|E_h|$ when $\omega = 40$, to clarify its direction.

The computational set-up for the solution of the inverse problem is as follows. We generate transmitted data by solving the model problem (45) on a three-times adaptively refined mesh. In this way, we avoid variational problems when we solve the inverse problem. The transmitted data are collected at receivers located at every point of the transmitted boundary $\partial_2\Omega$, and then normally distributed Gaussian noise $\delta = 3\%, 10\%$ with mean $\mu = 0$ is added to these data; see Figures 8d–f and 9d–f. The next step is data pre-processing: the noisy data are smoothed out; see Figures 8g–i and 9g–i. Next, to reconstruct ε_r, we minimize the Tikhonov functional (8). For the solution of the minimization problem, we introduce a Lagrangian and search for a stationary point of it using the adaptive Algorithm 4; see details in Section 4.6.

We take the initial approximation $\varepsilon_0 = 1$ at all points of the computational domain, which corresponds to the start of our computations from the homogeneous domain. This is done because of previous computational works [34], as well as the experimental works

of [6,8,10], where it was shown that such a choice gives good results in the reconstruction of the dielectric permittivity function.

5.3. Test 1

In this test, we present numerical results of the reconstruction of ε_r; exact values of this function are given in Table 1—see Test 1. The isosurface of the exact function ε_r to be reconstructed in this test is shown in Figure 7a. We note that the exact function ε_r has a complicated structure. Using Figure 7a, one can observe that the isosurface presents a discontinuous function with a number of large and small inclusions in the domain Ω_{FEM}.

Figure 11a–i show results of the reconstruction on adaptively locally refined meshes when the noise level in the data was $\delta = 10\%$. We start computations on a coarse mesh K_{h0}. Figure 11a–c show that the location of the reconstructed function ε_{h0} is imaged correctly and the reconstructed isosurface covers the domain where the exact ε_r is located. We refer to Table 2 for the reconstruction of the maximal contrast in ε_{h0}. For improvement of the contrast and shape obtained on a coarse mesh K_{h0}, we run computations on locally adaptively refined meshes. Figure 11d–f show the reconstruction obtained on the final two-times refined mesh K_{h2}. Table 2 presents results of reconstructions for ε_{hk} obtained on the refined meshes $K_{hk}, k = 0, 1, 2$. We observe that with mesh refinements, we achieve better contrast for function ε_r. Moreover, the reconstructed isosurface of this function more precisely covers the domain where the exact ε_r is located; compare Figure 11a with Figure 11d. Figure 11g–i show locally adaptively refined mesh K_{h2}.

Table 2. Test 1. Computational results of the reconstructions $\max_{\Omega_{\text{FEM}}} \varepsilon_{hk}$ on a coarse and on adaptively refined meshes together with relative errors computed in the maximal contrast of $\max_{\Omega_{\text{FEM}}} \varepsilon_r, \max_{\Omega_{\text{FEM}}} \varepsilon_{hk}$. Here, $\max_{\Omega_{\text{FEM}}} \varepsilon_{hk}$ denotes the maximum of the computed function ε_h on k-times refined mesh K_{hk} in the domain Ω_{FEM}, and M^k denotes the final number of iterations in the conjugate gradient Algorithm 3 on k-times refined mesh K_{hk} for reconstructed function $\varepsilon_{hk}, k = 0, 1, 2$.

Test 1							
$\delta = 3\%$				$\delta = 10\%$			
Mesh	$\max_{\Omega_{\text{FEM}}} \varepsilon_{hk}$	$\frac{\max_{\Omega_{\text{FEM}}} \lvert\varepsilon_r - \varepsilon_{hk}\rvert}{\max_{\Omega_{\text{FEM}}} \lvert\varepsilon_r\rvert}$	M^k	**Mesh**	$\max_{\Omega_{\text{FEM}}} \varepsilon_{hk}$	$\frac{\max_{\Omega_{\text{FEM}}} \lvert\varepsilon_r - \varepsilon_{hk}\rvert}{\max_{\Omega_{\text{FEM}}} \lvert\varepsilon_r\rvert}$	M^k
K_{h0}	6.535	0.274	2	K_{h0}	7.019	0.220	2
K_{h1}	7.865	0.126	2	K_{h1}	7.481	0.167	4
K_{h2}	10.0	0.111	2	K_{h2}	9.234	0.026	4

5.4. Test 2

Since it is quite demanding to reconstruct the very complicated structure of ε_r taken in Test 1, in this test, we will reconstruct ε_r with the exact isosurface as it is presented in Figure 7b. Exact values of this function are taken as in fibroconnective/glandular-1 media (see Table 1) inside the isosurface of Figure 7b, and outside of this isosurface, all values of $\varepsilon_r = 1$.

Figure 12a–i show results of the reconstruction on adaptively refined meshes when the noise level in the data was $\delta = 10\%$. We refer to Table 3 for the reconstruction of the contrast in ε_r. Using Table 3, we now observe that, with mesh refinements, we achieve slightly higher maximal contrast 9.45 in reconstruction ε_{h1} compared to the exact one 9. Moreover, on the mesh K_{h1} for $\sigma = 10\%$, we obtain a more than eight-times smaller relative error in the reconstruction compared to the error obtained on the coarse mesh K_{h0}. Figure 12d–i show good matching of the reconstructed ε_{h1} compared with the exact one. Figure 11j–l show locally adaptively refined mesh K_{h2}.

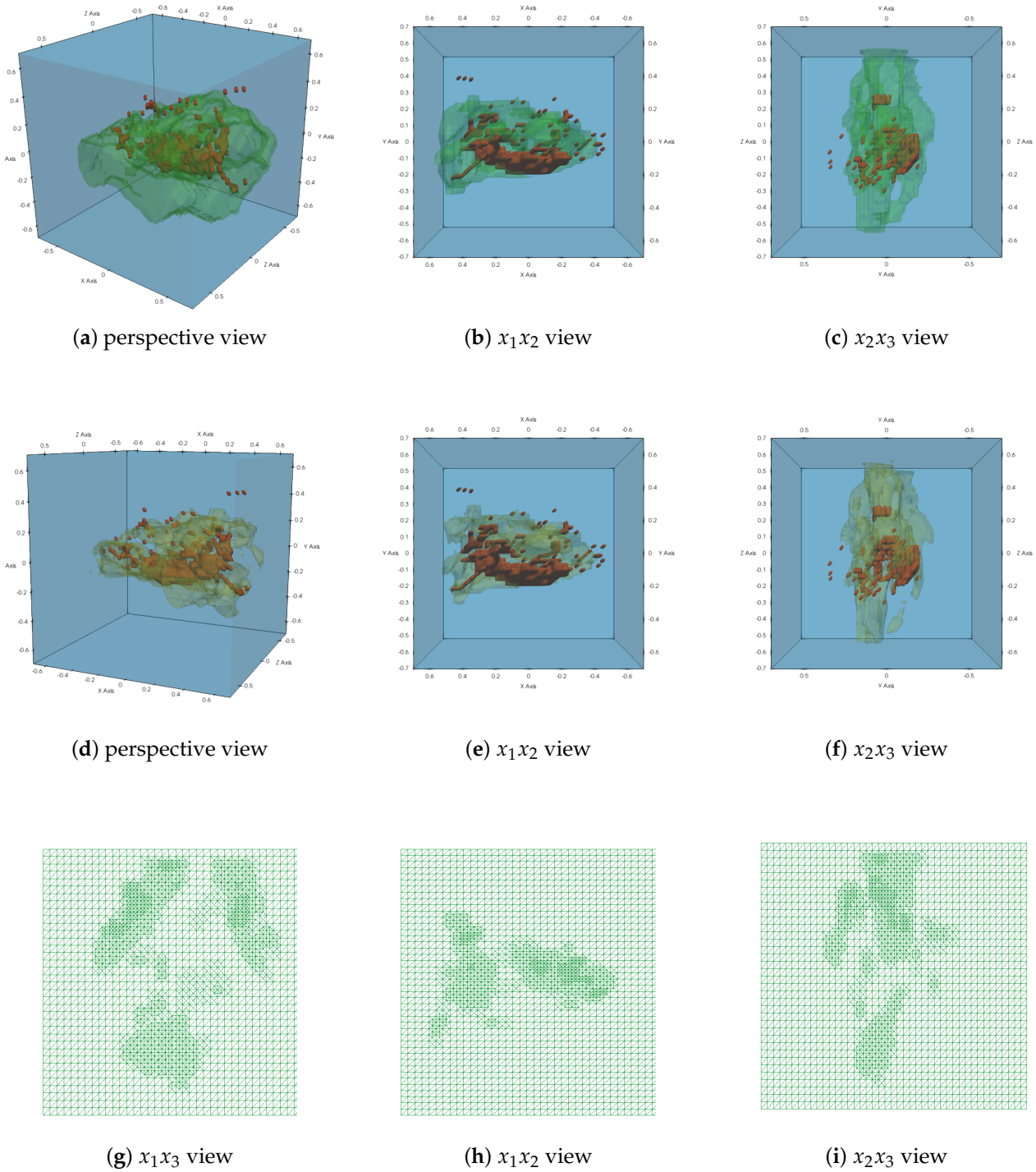

(**a**) perspective view (**b**) x_1x_2 view (**c**) x_2x_3 view

(**d**) perspective view (**e**) x_1x_2 view (**f**) x_2x_3 view

(**g**) x_1x_3 view (**h**) x_1x_2 view (**i**) x_2x_3 view

Figure 11. Test 1. (**a–c**): Reconstructions $\varepsilon_{h_0} \approx 5.0$ (outlined in transparent green color) of ε_r obtained on the coarse mesh. (**d–f**): Reconstructions $\varepsilon_{h2} \approx 5.0$ obtained on refined mesh K_{h2}. (**g–i**): refined mesh K_{h2}. The noise level in the data is $\delta = 10\%$. See Table 2 for obtained contrasts $\max_{\Omega_{\text{FEM}}} \varepsilon_{hk}, k = 0, 1, 2$. For comparison, we also present the exact isosurface with values corresponding to reconstructed ones and outlined in the red color.

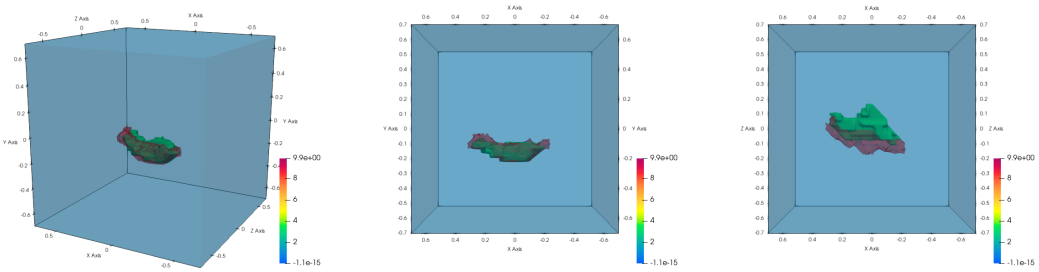

(**a**) prospect view (**b**) x_1x_2 view (**c**) x_1x_3 view

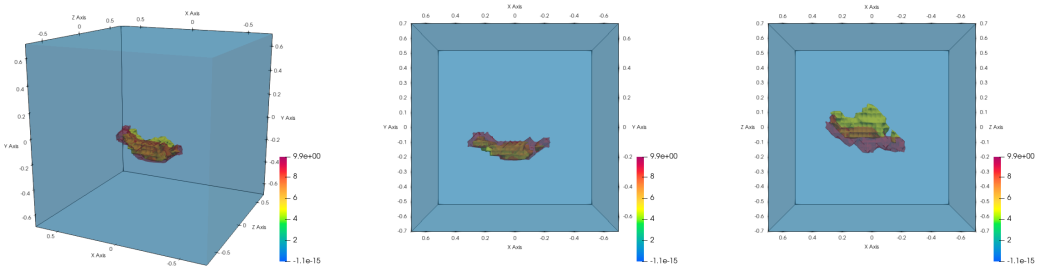

(**d**) prospect view (**e**) x_1x_2 view (**f**) x_1x_3 view

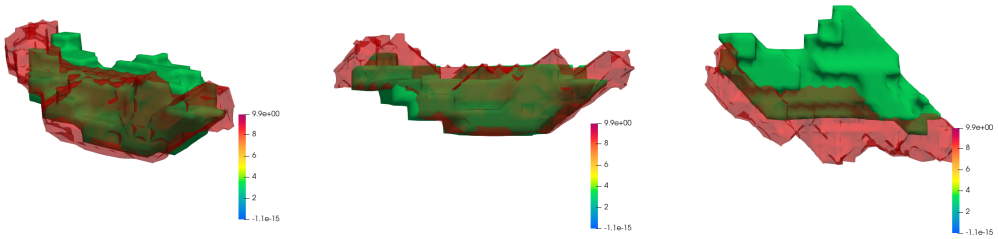

(**g**) zoomed prospect view (**h**) zoomed x_1x_2 view (**i**) zoomed x_1x_3 view

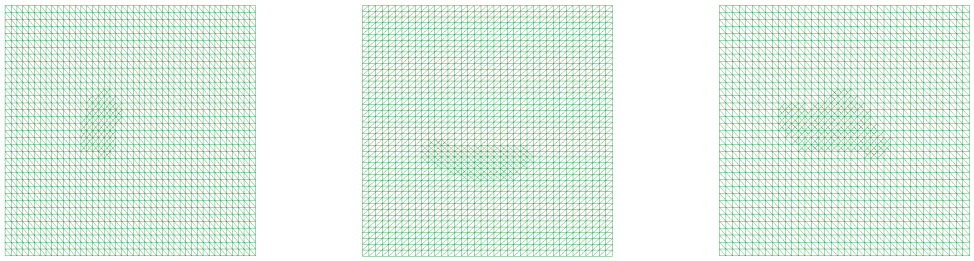

(**j**) x_2x_3 view (**k**) x_1x_2 view (**l**) x_1x_3 view

Figure 12. Test 2. (**a**–**c**): Isosurfaces of reconstructions $\varepsilon_{h_0} \approx 5.0$ (in green color) of ε_r obtained on the coarse mesh K_{h0}. (**d**–**f**): Isosurfaces of reconstructions $\varepsilon_{h1} \approx 5.0$ obtained on refined mesh K_{h1} (in yellow color). (**g**–**i**) Zoomed reconstructions. (**j**–**l**): Refined mesh K_{h1}. The noise level in the data is $\delta = 10\%$. See Table 3 for obtained contrasts $\max_{\Omega_{\text{FEM}}} \varepsilon_{hk}, k = 0, 1$. For comparison, we also present the exact isosurface of ε_r with values corresponding to reconstructed ones and outlined in the red color.

Table 3. Test 2. Computational results of the reconstructions $\max_{\Omega_{\text{FEM}}} \varepsilon_{hk}$ on a coarse and on adaptively refined meshes together with relative errors computed in the maximal contrast of $\max_{\Omega_{\text{FEM}}} \varepsilon_r$, $\max_{\Omega_{\text{FEM}}} \varepsilon_{hk}$. Here, $\max_{\Omega_{\text{FEM}}} \varepsilon_{hk}$ denotes the maximum of the computed function ε_h on k-times refined mesh K_{hk} in the domain Ω_{FEM}, and M^k denotes the final number of iterations in the conjugate gradient Algorithm 3 on k-times refined mesh K_{hk} for reconstructed function $\varepsilon_{hk}, k = 0, 1, 2$.

Test 2							
$\delta = 3\%$				$\delta = 10\%$			
Mesh	$\max_{\Omega_{\text{FEM}}} \varepsilon_{hk}$	$\frac{\max_{\Omega_{\text{FEM}}} \lvert\varepsilon_r - \varepsilon_{hk}\rvert}{\max_{\Omega_{\text{FEM}}} \lvert\varepsilon_r\rvert}$	M^k	**Mesh**	$\max_{\Omega_{\text{FEM}}} \varepsilon_{hk}$	$\frac{\max_{\Omega_{\text{FEM}}} \lvert\varepsilon_r - \varepsilon_{hk}\rvert}{\max_{\Omega_{\text{FEM}}} \lvert\varepsilon_r\rvert}$	M^k
K_{h0}	6.874	0.236	2	K_{h0}	5.350	0.406	2
K_{h1}	7.558	0.160	5	K_{h1}	9.450	0.05	4
K_{h2}	10.0	0.111	2				

5.5. Performance Comparison

All computations were performed on a Linux workstation with an Intel Core i7-9700 CPU with one processor using software package WavES [44], efficiently implemented in C++/PETSc [45].

We have estimated the relative computational time T_r of the forward problem using the following formula:

$$T_r = \frac{t}{n_t \cdot n}. \tag{48}$$

Here, t is the total computational time of the forward problem on the mesh K_{hl}, where $l = 0, 1, 2, \ldots$ is the number of the refined mesh, n is the total number of nodes in the mesh K_{hl}, and n_t is the number of time steps. We take $n_t = 500$ in all computational tests; see clarification in Section 5.2. Computational times (in seconds) for the solution of the forward problem are presented in Table 4. Using this table, we observe that the relative time is approximately the same for all tests and we can take it as $T_r \approx 1.8 \times 10^{-6}$. Next, using this relative time, we can estimate the approximate computational time for the solution of the forward problem for any mesh consisting of n nodes. For example, if we take the original mesh consisting of $n = 34,036,992$ nodes, then the computational time will be already $t = T_r \times n_t \times n = 1.8 \times 10^{-6} \times 500 \times 34,036,992 = 30,633$ s, and this time is not computationally efficient. Clearly, the computation of the solution of the inverse problem on the sampled mesh allows significantly reduced computational times.

Table 4. Performance of solution of forward problem (45) in Tests 1 and 2 of Section 5 on the mesh K_{h0} in terms of computational time (in seconds) and relative computational time computed by (48). Here, n is the number of the nodes on the three-times adaptively refined original coarse mesh (consisting of 63,492 nodes), which we used for the generation of transmitted data.

Computational Time							
$\delta = 3\%$				$\delta = 10\%$			
	Time (s)	**Relative Time**	n	**Time (s)**	**Relative Time**	n	
Test 1	110.59	1.779×10^{-6}	71,360	Test 1	116.22	1.869×10^{-6}	75,052
Test 2	106.58	1.714×10^{-6}	69,699	Test 2	111.53	1.793×10^{-6}	65,359

We have estimated also the relative computational time T_r^{ip} of the solution of the inverse problem using the formula

$$T_r^{ip} = \frac{t^{ip}}{n_t \cdot nno}. \tag{49}$$

Here, t^{ip} is the total computational time to run inverse Algorithm 4 on the mesh K_{hl}, where $l = 0, 1, 2, \ldots$ is the number of the refined mesh, *nno* is the total number of nodes in the mesh K_{hl}, and n_t is number of time steps. Computational times (in seconds) for the solution of the inverse problem for Test 1 and Test 2 are presented in Tables 5 and 6, respectively. Using these tables, we observe that the computational times are dependent on the number of iterations M^k in the conjugate gradient method (CGM) and the number of nodes *nno* in the meshes K_{hl}. We took $n_t = 500$ for all tests and, thus, the computational times presented in these tables are not dependent on the number of time steps for different refined meshes. We note that the number of time steps n_t can be chosen adaptively as well. However, we perform adaptive mesh refinement in space only, and not in time. The full space–time adaptive algorithm can be considered as a topic for future research.

Using Table 5, we observe that the computational time in Test 1 is around 20 min for both noise levels $\sigma = 3\%$ and $\sigma = 10\%$. On every mesh $K_{hl}, l = 0, 1, 2$, we performed two iterations of CGM, or $M^K = 2$. Thus, the total computational time to obtain the final reconstruction in Test 1 is 60 min.

Table 6 shows that the computational time in Test 2 with noise in data $\delta = 3\%$ is around 20 min for non-refined mesh K_{h0}, 60 min for one-time refined mesh K_{h1}, and 20 min for twice-refined mesh K_{h2}. Thus, the total computational time to obtain the final reconstruction in Test 2 is 100 min. The computational time in this test is greater than in the previous Test 1 since CGM converged only at the fifth iteration on the one-time refined mesh K_{h1}. However, the total computational time with noise in data $\delta = 10\%$ is around 60 min. This is because the solution was obtained already on the one-time refined mesh K_{h1}. Tables 5 and 6 also demonstrate that it takes around 10 min to compute the solution of the inverse problem on the one iteration of the conjugate gradient algorithm.

We note that PETSc supports parallel implementation and, thus, the current version of the code can be extended to the version with parallel implementation such that the times reported in Tables 4–6 can be significantly reduced.

Table 5. Test 1. Performance of the reconstruction Algorithm 4 (in seconds) on adaptively refined meshes. Here, k is the number of the refined mesh K_{hk} of the domain Ω_{FEM}, *nno* is the number of nodes in the computational mesh K_{hk}, and M^k denotes the final number of iterations in the conjugate gradient Algorithm 3.

Test 1, Computational Time									
	$\delta = 3\%$					$\delta = 10\%$			
Mesh	***nno***	**Time (s)**	**Rel. Time**	M^k	**Mesh**	***nno***	**Time (s)**	**Rel. Time**	M^k
K_{h0}	63,492	1183	3.73×10^{-5}	2	K_{h0}	63,492	1180	3.71×10^{-5}	2
K_{h1}	64,206	1199	3.74×10^{-5}	2	K_{h1}	64,766	2415	7.43×10^{-5}	4
K_{h2}	65,284	1212	3.71×10^{-5}	2	K_{h2}	67,965	2525	7.435×10^{-5}	4

Table 6. Test 2. Performance of the reconstruction Algorithm 4 (in seconds) on adaptively refined meshes. Here, k is the number of the refined mesh K_{hk} of the domain Ω_{FEM}, *nno* is the number of nodes in the computational mesh K_{hk}, and M^k denotes the final number of iterations in the conjugate gradient Algorithm 3.

Test 2, Computational Time									
	$\delta = 3\%$					$\delta = 10\%$			
Mesh	***nno***	**Time (s)**	**Rel. Time**	M^k	**Mesh**	***nno***	**Time (s)**	**Rel. Time**	M^k
K_{h0}	63,492	1186	3.72×10^{-5}	2	K_{h0}	63,492	1214	3.82×10^{-5}	2
K_{h1}	64,096	3588	9.34×10^{-5}	5	K_{h1}	63,968	2384	7.44×10^{-5}	4
K_{h2}	66,112	1228	3.72×10^{-5}	2					

6. Conclusions

This work describes reconstruction methods for the determination of the relative dielectric permittivity function in conductive media using scattered data of the time-dependent electric field at a number of detectors placed at the boundary of the investigated domain.

Reconstruction methods use an optimization approach where a functional is minimized via a domain decomposition finite element/finite difference method. In an adaptive reconstruction method, the space mesh is refined only in the domain where a finite element method is used, with feedback from a posteriori error indicators. The developed adaptive algorithms allow us to obtain the correct values and shapes of the dielectric permittivity function to be determined. Convergence and stability analysis of the developed methods is ongoing work and will be presented in a forthcoming publication. The algorithms of the current work are designed from previous adaptive algorithms developed in [16,34], which reconstruct the wave speed or the dielectric permittivity function. However, all previous algorithms are developed for non-conductive media.

Our computational tests show the qualitative and quantitative reconstruction of the dielectric permittivity function using an anatomically realistic breast phantom that captures the heterogeneity of normal breast tissue at a frequency of 6 GHz, taken from online repository [1]. In all tests, we used the assumption that the conductivity function is known. Currently, we are working on algorithms in which both dielectric permittivity and conductivity functions can be reconstructed. Results of this work will be presented in a future publication.

All computations were performed in real time and are presented in Tables 4–6. Some data (Matlab code to read data of database [1], visualize and produce discretized values of ε_r, σ, etc.) used in the computations of this work are available for download and testing; see [42]. Additional data (computational FE/FD meshes, transmitted data, C++/PETSc code) can be provided upon request.

In summary, the main features of the algorithms of this work are as follows:

- Ability to reconstruct shapes, locations and maximal values of dielectric permittivity function of targets in conductive media under the condition that the conductivity of this media is a known function.
- More exact reconstruction of shapes and maximal values of dielectric permittivity function of inclusions because of local adaptive mesh refinement.
- Computationally greater efficiency because of usage of software package WavES [44], implemented in C++/PETSc [45].

Author Contributions: Conceptualization, L.B., methodology, L.B., software, L.B., validation, L.B., E.L., investigation, L.B., E.L., data curation, L.B., E.L., writing—original draft preparation, L.B., E.L., writing—review and editing, L.B., E.L., visualization, L.B., E.L. All authors have read and agreed to the published version of the manuscript.

Funding: The research of authors is supported by the Swedish Research Council grant VR 2018-03661.

Institutional Review Board Statement: Not applicable.

Informed Consent Statement: Not applicable.

Data Availability Statement: Data available in a publicly accessible repository that does not issue DOIs Publicly available datasets were analyzed in this study. This data can be found here: github.com/ProjectWaves24/DDFEMFDMMaxwell/ (accessed on 1 March 2022).

Conflicts of Interest: The authors declare no conflict of interest.

References

1. Zastrow, E.; Davis, S.K.; Lazebnik, M.; Kelcz, F.; Veen, B.D.; Hageness, S.C. Online Repository of 3D Grid Based Numerical Phantoms for Use in Computational Electromagnetics Simulations. Available online: https://uwcem.ece.wisc.edu/MRIdatabase/ (accessed on 1 March 2022).
2. Joines, W.T.; Zhang, Y.; Li, C.; Jirtle, R.L. The measured electrical properties of normal and malignant human tissues from 50 to 900 MHz. *Med. Phys.* **1994**, *21*, 547–550. [CrossRef] [PubMed]
3. Chew, W.C.; Wang, Y.M. Reconstruction of two-dimensional permittivity distribution using the distorted Born iterative method. *IEEE Trans. Med. Imaging* **1990**, *9*, 218–225. [CrossRef]
4. Bulyshev, A.E.; Souvorov, A.E.; Semenov, S.Y.; Posukh, V.G.; Sizov, Y.E. Three-dimensional vector microwave tomography: Theory and computational experiments. *Inverse Probl.* **2004**, *20*, 1239–1259. [CrossRef]
5. Cuccaro, A.; Dell'Aversano, A.; Ruvio, G.; Browne, J.; Solimene, R. Incoherent Radar Imaging for Breast Cancer Detection and Experimental Validation against 3D Multimodal Breast Phantoms. *J. Imaging* **2021**, *7*, 23. [CrossRef] [PubMed]
6. Joachimowicz, N.; Pichot, C.; Hugonin, J.P. Inverse scattering: And iterative numerical method for electromagnetic imaging. *IEEE Trans. Antennas Propag.* **1991**, *39*, 1742–1753. [CrossRef]
7. Khoa, V.A.; Bidney, G.W.; Klibanov, M.V.; Nguyen, L.H.; Nguyen, L.H.; Sullivan, A.J.; Astratov, V.N. An inverse problem of a simultaneous reconstruction of the dielectric constant and conductivity from experimental backscattering data. *Inverse Probl. Sci. Eng.* **2021**, *29*, 712–735. [CrossRef]
8. Poplack, S.P.; Tosteson, T.D.; Wells, W.A.; Pogue, B.W.; Meaney, P.M.; Hartov, A.; Kogel, C.A.; Soho, S.K.; Gibson, J.J.; Paulsen, K.D. Electromagnetic Breast Imaging: Results of a Pilot Study in Women with Abnormal Mammograms. *Radiology* **2007**, *243*, 350–359. [CrossRef]
9. Zeng, X.; Fhager, A.; He, Z.; Persson, M.; Linner, P.; Zirath, H. Development of a Time Domain Microwave System for Medical Diagnostics. *IEEE Trans. Instrum. Meas.* **2014**, *63*, 2931–2939. [CrossRef]
10. Grzegorczyk, T.M.; Meaney, P.M.; Kaufman, P.A.; Alexander, R.M.D.; Paulsen, K.D. Fast 3-d tomographic microwave imaging for breast cancer detection. *IEEE Trans. Med. Imaging* **2012**, *31*, 1584–1592. [CrossRef] [PubMed]
11. Bakushinsky, A.B.; Kokurin, M.Y. *Iterative Methods for Approximate Solution of Inverse Problems*; Springer: Dordrecht, The Netherlands, 2004.
12. Kabanikhin, S.; Satybaev, A.; Shishlenin, M. *Direct Methods of Solving Multidimensional Inverse Hyperbolic Problems*; VSP: Ultrecht, The Netherlands, 2004.
13. Tikhonov, A.N.; Goncharsky, A.V.; Stepanov, V.V.; Yagola, A.G. *Numerical Methods for the Solution of Ill-Posed Problems*; Kluwer: London, UK, 1995.
14. Ito, K.; Jin, B. *Inverse Problems: Tikhonov Theory and Algorithms*; Series on Applied Mathematics; World Scientific: Singapore, 2015; Volume 22.
15. Beilina, L.; Klibanov, M.V. *Approximate Global Convergence and Adaptivity for Coefficient Inverse Problems*; Springer: New York, NY, USA, 2012.
16. Beilina, L.; Th'anh, N.T.; Klibanov, M.V.; Malmberg, J.B. Globally convergent and adaptive finite element methods in imaging of buried objects from experimental backscattering radar measurements. *J. Comput. Appl. Math.* **2015**, *289*, 371–391. [CrossRef]
17. Thánh, N.T.; Beilina, L.; Klibanov, M.V.; Fiddy, M.A. Reconstruction of the refractive index from experimental backscattering data using a globally convergent inverse method. *SIAMJ. Sci. Comput.* **2014**, *36*, B273–B293. [CrossRef]
18. Thánh, N.T.; Beilina, L.; Klibanov, M.V.; Fiddy, M.A. Imaging of Buried Objects from Experimental Backscattering Time-Dependent Measurements using a Globally Convergent Inverse Algorithm. *SIAM J. Imaging Sci.* **2015**, *8*, 757–786. [CrossRef]
19. Aram, M.G.; Beilina, L.; Trefna, H.D. Microwave Thermometry with Potential Application in Non-invasive Monitoring of Hyperthermia. *J. Inverse Ill-Posed Probl.* **2020**, *28*, 739–750. [CrossRef]
20. Solimene, R.; Cuccaro, A.; Ruvio, G.; Tapia, D.F.; Halloran, M.O. Beamforming and Holography Image Formation Methods: An Analytic Study. *Opt. Express* **2016**, *24*, 9077–9093. [CrossRef] [PubMed]
21. Klibanov, M.V.; Li, J. *Inverse Problems and Carleman Estimates: Global Uniqueness, Global Convergence and Experimental Data*; De Gruyter: Berlin, Germany; Boston, MA, USA, 2021. [CrossRef]
22. Křížek, M.; Neittaanmäki, P. *Finite Element Approximation of Variational Problems and Applications*; Longman: Harlow, UK, 1990.
23. Engquist, B.; Majda, A. Absorbing boundary conditions for the numerical simulation of waves. *Math. Comp.* **1977**, *31*, 629–651. [CrossRef]
24. Monk, P.B. *Finite Element Methods for Maxwell's Equations*; Oxford University Press: Oxford, UK, 2003.
25. Nédélec, J.-C. Mixed finite elements in R3. *Numer. Math.* **1980**, *35*, 315–341. [CrossRef]
26. Elmkies, A.; Joly, P. Finite elements and mass lumping for Maxwell's equations: The 2D case. *Comptes Rendus L'Academie Des Sci. Ser. Math.* **1997**, *324*, 1287–1293.
27. Joly, P. *Variational Methods for Time-Dependent Wave Propagation Problems*; Lecture Notes in Computational Science and Engineering; Springer: Berlin/Heidelberg, Germany, 2003.
28. Monk, P.B.; Parrott, A.K. A dispersion analysis of finite element methods for Maxwell's equations. *SIAM J. Sci. Comput.* **1994**, *15*, 916–937. [CrossRef]
29. Paulsen, K.D.; Lynch, D.R. Elimination of vector parasites in Finite Element Maxwell solutions. *IEEE Trans. Microw. Theory Technol.* **1991**, *39*, 395–404. [CrossRef]

30. Jiang, B. *The Least-Squares Finite Element Method. Theory and Applications in Computational Fluid Dynamics and Electromagnetics*; Springer: Heidelberg, Germany, 1998.
31. Jiang, B.; Wu, J.; Povinelli, L.A. The origin of spurious solutions in computational electromagnetics. *J. Comput. Phys.* **1996**, *125*, 104–123. [CrossRef]
32. Jin, J. *The Finite Element Method in Electromagnetics*; Wiley: New York, NY, USA, 1993.
33. Munz, C.D.; Omnes, P.; Schneider, R.; Sonnendrucker, E.; Voss, U. Divergence correction techniques for Maxwell Solvers based on a hyperbolic model. *J. Comput. Phys.* **2000**, *161*, 484–511. [CrossRef]
34. Malmberg, J.B.; Beilina, L. An Adaptive Finite Element Method in Quantitative Reconstruction of Small Inclusions from Limited Observations. *Appl. Math. Inf. Sci.* **2018**, *12*, 1–19. [CrossRef]
35. Beilina, L. Energy estimates and numerical verification of the stabilized Domain Decomposition Finite Element/Finite Difference approach for time-dependent Maxwell's system. *Cent. Eur. J. Math.* **2013**, *11*, 702–733. [CrossRef]
36. Beilina, L.; Ruas, V. *Convergence of Explicit P1 Finite-Element Solutions to Maxwell's Equations*; Springer Proceedings in Mathematics and Statistics; Springer: Cham, Switzerland, 2020; Volume 328.
37. Brenner, S.C.; Scott, L.R. *The Mathematical Theory of Finite Element Methods*; Springer: Berlin, Germany, 1994.
38. Cohen, G.C. *Higher Order Numerical Methods for Transient Wave Equations*; Springer: Berlin, Germany, 2002.
39. Pironneau, O. *Optimal Shape Design for Elliptic Systems*; Springer: Berlin, Germany, 1984.
40. Lazebnik, M.; McCartney, L.; Popovic, D.; Watkins, C.B.; Lindstrom, M.J.; Harter, J.; Sewall, S.; Magliocco, A.; Booske, J.H.; Okoniewski, M.; et al. A large-scale study of the ultrawideband microwave dielectric properties of normal breast tissue obtained from reduction surgeries. *Phys. Med. Biol.* **2007**, *52*, 2637–2656. [CrossRef]
41. Lazebnik, M.; Popovic, D.; McCartney, L.; Watkins, C.B.; Lindstrom, M.J.; Harter, J.; Sewall, S.; Ogilvie, T.; Magliocco, A.; Breslin, T.M.; et al. A large-scale study of the ultrawideband microwave dielectric properties of normal, benign, and malignant breast tissues obtained from cancer surgeries. *Phys. Med. Biol.* **2007**, *52*, 6093–6115. [CrossRef]
42. WavES, DD FEM/FDM for Time-Dependent Maxwell's Equations, Data Repository. Available online: github.com/ProjectWaves24/DDFEMFDMMaxwell (accessed on 1 March 2022).
43. Romanov, V.G.; Klibanov, M.V. Can a single PDE govern well the propagation of the electric wave field in a heterogeneous medium in 3D? *arXiv* **2021**, arXiv:2102.02271.
44. WavES, the Software Package. Available online: http://www.waves24.com/ (accessed on 1 March 2022).
45. Portable, Extensible Toolkit for Scientific Computation PETSc. Available online: http://www.mcs.anl.gov/petsc/ (accessed on 1 March 2022).